Non-Rigid Registration Via Intelligent Adaptive Feedback Control

Tajdari, Farzam; Huysmans, Toon; Song, Yu

DOI
10.1109/TVCG.2023.3283990

Publication date
2024

Document Version
Final published version

Published in
IEEE Transactions on Visualization and Computer Graphics

Citation (APA)
Tajdari, F., Huysmans, T., & Song, Y. (2024). Non-Rigid Registration Via Intelligent Adaptive Feedback Control. *IEEE Transactions on Visualization and Computer Graphics*, *30*(8), 4910-4926. https://doi.org/10.1109/TVCG.2023.3283990

Non-Rigid Registration Via Intelligent Adaptive Feedback Control

Farzam Tajdari, Toon Huysmans, and Yu Song, *Member, IEEE*

***Abstract*—Preserving features or local shape characteristics of a mesh using conventional non-rigid registration methods is always difficult, as the preservation and deformation are competing with each other. The challenge is to find a balance between these two terms in the process of the registration, especially in presence of artefacts in the mesh. We present a non-rigid Iterative Closest Points (ICP) algorithm which addresses the challenge as a control problem. An adaptive feedback control scheme with global asymptotic stability is derived to control the stiffness ratio for maximum feature preservation and minimum mesh quality loss during the registration process. A cost function is formulated with the distance term and the stiffness term where the initial stiffness ratio value is defined by an Adaptive Neuro-Fuzzy Inference System (ANFIS)-based predictor regarding the source mesh and the target mesh topology, and the distance between the correspondences. During the registration process, the stiffness ratio of each vertex is continuously adjusted by the intrinsic information, represented by shape descriptors, of the surrounding surface as well as the steps in the registration process. Besides, the estimated process-dependent stiffness ratios are used as dynamic weights for establishing the correspondences in each step of the registration. Experiments on simple geometric shapes as well as 3D scanning datasets indicated that the proposed approach outperforms current methodologies, especially for the regions where features are not eminent and/or there exist interferences between/among features, due to its ability to embed the inherent properties of the surface in the process of the mesh registration.**

***Index Terms*—Adaptive control, global asymptotic stability, ANFIS predictor, mesh quality, shape descriptor, non-rigid registration.**

I. INTRODUCTION

In THE past decades, non-rigid registration is widely used in many applications like motion and shape analysis [1], [2], image registration for medical purposes [3], [4], etc. Although there are many forms of non-rigid mesh registration algorithms, the non-rigid Iterative Closest Point (ICP) registration drew more attention, as it is simple in the implementation with high efficiency and effectiveness regarding different types of applications [5]. Currently, non-rigid ICP was employed in a number of applications, e.g. statistical shape analysis [6], [7], computer vision [8], multimedia applications [9], and 3D geometry of human body analysis [10], [11], [12].

The non-rigid ICP registration is presented as a non-trivial and ill-defined problem, which contains a high number of Degrees-Of-Freedom (DOFs). Thus, preserving features of the source surface during the registration process in the formulation of the algorithm [13] with respect to the topology of the target surface is always challenging. For example, creating meaningful robust correspondences in each step of the iteration [14], defining the unique time-varying stiffness level per vertex to maximize feature preservation and minimize mesh quality loss, and establishing the convergence regarding the suited minimum in the process of optimization [15]. Here, the features are defined as salient geometric characteristics [16], e.g. curvature.

Researchers utilized different approaches to tackle those challenges, i.e., utilizing landmarks (LMs) to enhance the corresponding selection [17], [18], [19], [20], embedding an adaptive template [21], adding more terms representing shape characteristics in the cost functions [22], and using controlled point-based transformation, e.g. generalizing the affine model from linear to non-linear case [23] to have a more reasonable deformation. Although the aforementioned approaches could accurately determine the pattern of non-linear deformation among meshes to be registered, the challenges are not fully addressed, mainly due to the difficulty in balancing the desired non-rigid deformation and the preservation of salient features across the complete registration process.

To address the balance of several competing terms, researchers developed different methods capable of simultaneously controlling and identifying the unknown parameters of a system online (see, e.g., [24]), which could be integrated into the non-rigid registration methods as a controller scheme controlling the feature preservation and mesh quality by identifying the level of ”stiffness per vertex”. ”Stiffness per vertex” is the stiffness degree that a vertex has with its one-ring neighboring points. Therefore, the challenge can be formulated as a control problem in the scenario where the model structure is assumed known and parameters’ values are unknown. A possible method to solve the problem is the Model Reference Adaptive Control (MRAC),

Manuscript received 12 April 2022; revised 11 May 2023; accepted 24 May 2023. Date of publication 8 June 2023; date of current version 1 July 2024. This work was supported by Dutch NWO Next UPPS - Integrated design methodology for Ultra Personalised Products and Services project under Grant 15470. Recommended for acceptance by A. Vaxman. *(Corresponding author: Farzam Tajdari.)*

Farzam Tajdari is with the Faculty of Industrial Design Engineering, Delft University of Technology, 2628 Delft, The Netherlands, and also with the Department of Mechanical Engineering, Dynamics and Control (D&C) group, Technical University of Eindhoven, 5612 Eindhoven, AZ, The Netherlands (e-mail: f.tajdari@tudelft.nl).

Toon Huysmans is with the Faculty of Industrial Design Engineering, Delft University of Technology, 2628 Delft, The Netherlands, and also with the Imec-Vision Lab, Department of Physics, University of Antwerp, 2000 Antwerpen, Belgium (e-mail: t.huysmans@tudelft.nl).

Yu Song is with the Faculty of Industrial Design Engineering, Delft University of Technology, 2628 Delft, The Netherlands (e-mail: y.song@tudelft.nl).

Digital Object Identifier 10.1109/TVCG.2023.3283990

which is designed to exploit conventional controllers while the controllers' parameters are updated based on model parameters identification. Though such methods have been widely used in controlling robotic systems [25], [26], online identification [27], [28], and noise filtering [29], etc. the use of MRAC in the area of non-rigid registration, e.g., mesh registration, is rare.

This paper presents a novel globally robust approach for estimating the level of stiffness per vertex in each iteration of the non-rigid ICP via an intelligent MRAC framework to maximally preserve features with minimized mesh quality loss. In fact, here, we are addressing the establishment of a direct compromise between the level of deformation and preserving features per vertex; however, our previous work in [30] elaborates on first introducing a nonlinear shape descriptor to distinguish corresponding points, namely semi-curvature term, and then establishing a framework to solve a nonlinear problem with a linear optimizer. The method in our previous work [30] was ill to address the optimum registration at vertex level, especially for the missing parts of the target surface, e.g. excessive deformation resulting in large triangles covering the missing parts and small needle-like triangles at the edges of the missing parts. The main scientific contributions of this paper are:

- We introduce an adaptive stiffness ratio estimator utilizing the intrinsic information of the surface to establish the correspondence as well as adjust the stiffness term in each step of the non-rigid ICP registration for better preservation of the shape properties;
- We prove that the estimator is globally asymptotically stable through a Lyapunov function;
- We integrate a data-driven ANFIS-based method to suggest the initial stiffness ratio values of the estimator to further improve the effectiveness and efficiency.

II. RELATED WORK

In non-rigid ICP registrations, the relationships between similar features on the source and the target surfaces are often used to establish meaningful dense correspondences. Besides manual labelling, pattern recognition techniques are also employed to automatically specify LMs, e.g., [17], [18], [19], [20]. However, those LMs are mostly positioned at the extrema of specific shape descriptors which are scarcely scattered across the surface and cannot describe the complete spectrum of the inherent properties of the surface. To embed extra features inside the registration algorithms, researchers investigated various inherent properties in the selection of correspondence. An iterative registration approach introduced in [21] combined ICP with Coherent Point Drift (CPD) to have a more robust correspondence selection. Recently, a Bayesian Coherent Point Drift (BCPD) method in [31] integrated the coherent drift in the variational Bayesian inference theory, while maintaining the rudimentary characteristics of the CPD method. In [32], a rigid ICP registration technique was introduced, employing curvature value resemblance to establish correspondences. However, the approach is sensitive to noise, and the computing time is exponentially growing regarding the number of vertices in the surfaces. Recently, a new semi-curvature term is introduced in [30] which considerably improved the corresponding selection accuracy. However, it was sensitive to the border shapes of an open mesh.

Shape characteristics may disappear when the output of non-rigid registration is very smooth, e.g. due to the inclusion of a smoothness functional in the cost function. For preserving the mesh quality of the surface, integrating regularization terms, e.g. ℓ_2-norm term [33], in the structure of the cost function helps. For example, Amberg et al. [34] presented an ℓ_2-norm cost function integrated with a stiffness term to maintain local mesh quality. Yang et al. [35] also used a sparse non-rigid registration scheme through an ℓ_1-norm cost function for feature preservation. However, the constraints of the position (e.g. adjacent piece-wise rigid deformation) were not adequately integrated with the model to incorporate the association with the piece-wise rigid deformation. Recently, Ayan [36] proposed a registration methodology utilizing an energy function incorporating the strength of local and global geometry through an intermediate level depiction of the point cloud. However, the approach is sensitive to the point density areas with detailed geometry features.

During an iterative non-rigid registration process, once the corresponding points are defined in each iteration, the path from the current condition of the points on the source mesh to the corresponded points on the target mesh is very challenging as the level of deformation to the corresponding point and level of the mesh quality are in contrast with each other. Thus, an optimal path should be capable to be adaptively updated in each iteration to allow for sufficient deformation per vertex while safeguarding the mesh quality of faces. As the solution is feedback-based, adaptive feedback control approaches might be a problem solver. Adaptive solutions have vast applications such as 3D meshing [37], [38], and mesh refinement [39]; however, there is no prior work about adaptive feedback solutions or adaptive control for 3D mesh registration. Instead, there are limited research works regarding adaptive image registration. In the area of adaptive image registration, non-rigid registration employing Radial Basis Functions (RBFs) [40], [41], [42] are interesting as they are meshless. In theory, knots can be located optimally and adaptively for a deformation area to reach the acceptable accuracy. Zhou et al. [43] proposed a RBF-based approach to address non-correspondent point-clouds registration. Recently, Zhang et al. [44] presented an implementation of RBF non-rigid registration with iterative knot-placement to adaptively decrease registration local error. However, quantitative evaluation of accuracy was lacking in RBF-based methods.

III. METHODOLOGY

A. Problem Formulation

In the context of non-rigid registration, most of the available methods try to non-rigidly align a point cloud to the other point cloud in which this alignment accompanies deformation. However, in those methods, the meaning of the ideal deformation is vague and usually defined as reaching the least geometry error with the corresponding points; however, the deformation can destroy some features in the source mesh and/or reduce the quality of the source mesh. The biggest challenge here is that the

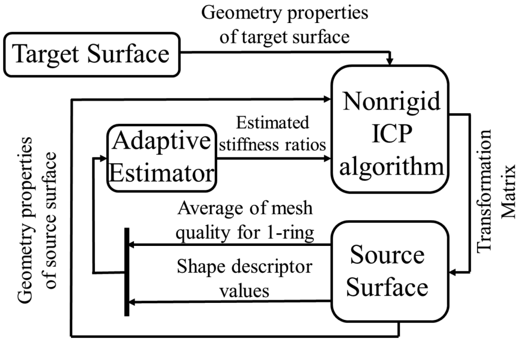

Fig. 1. Non-rigid ICP and the adaptive estimator integration diagram. The feedback-based estimator adjusts the proper stiffness ratio per vertex, to minimize the mesh quality loss, and preserve the maximum possible feature of the source mesh.

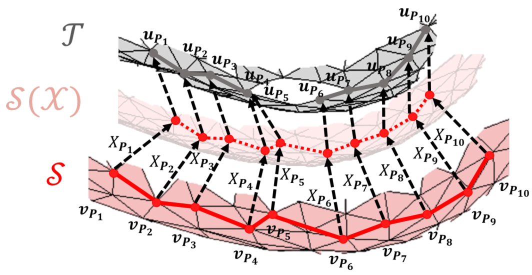

Fig. 2. Non-rigidly registering the source surface to the target surface.

methods use similar parameter values for all the points on the source mesh during registration, while each point in fact needs an advanced investigation based on its condition, to set those values. Thus, online parameter tuning for each vertex based on the course of registration for the vertex is a key to the challenge. To this end, a method that can optimize the degree of deformation in order to minimize the geometry error and maximize the degree of feature preservation is a breakthrough. In this paper, we introduce a novel method to adjust those parameters per-vertex online and implement it on the most simple registration method of ICP to study the impact of our method on the quality of registration. Instead of using the same values for the stiffness term value, we propose an adaptive estimator for generating proper vertex-wise stiffness values for the source surface. The procedure is depicted in Fig. 1, and the used variables and parameters are reported in Table I. According to the figure, in each iteration of the optimization process in the non-rigid ICP algorithm, the feedback-based adaptive estimator defines the proper stiffness ratio per vertex using the geometry properties of the source surface, namely shape descriptor value and average of mesh quality, to maintain the highest possible deformation with the least source surface feature loss.

B. Non-Rigid ICP Registration

During the non-rigid ICP registration, $\mathcal{S} = (\mathcal{V}, \mathcal{E})$ as the source surface, with n vertices in $\mathcal{V}$ and m edges in $\mathcal{E}$, is iteratively registered to the target surface $\mathcal{T}$. Fig. 2 demonstrates one step of the registration process.

TABLE I
USED VARIABLES AND PARAMETERS

Symbol	Description
	The ICP method
$\mathcal{S}$	Source surface
$\mathcal{T}$	Target surface
n	Number of vertices on $\mathcal{S}$
$n_\mathcal{T}$	Number of vertices on $\mathcal{T}$
P_i	An arbitrary point on $\mathcal{S}$
v_{P_i}	Geometry of P_i on $\mathcal{S}$
u_{P_i}	Geometry of Corresponding point to v_{P_i} on $\mathcal{T}$
X_{P_i}	Transformation matrix for P_i
D	A matrix including geometry of all points on $\mathcal{S}$
U	A matrix including all the points on $\mathcal{T}$
$\tilde{U}$	A matrix including corresponding points from $\mathcal{S}$ to $\mathcal{T}$
G	Stiffness weighting matrix
	The adaptive Estimator
e_s	Integral error of shape descriptor for P_i
e_q	Integral error of average of mesh quality for P_i
k_s^t	Shape descriptor value at time t
k_s^0	Shape descriptor value before registration
q^t	Average of mesh quality value at time t
q^0	Average of mesh quality value before registration
t	Index of time (iterations)
$\tilde{a}$	Vector of unknown parameters
$\hat{g}_{P_i}$	Estimating unknown stiffness ratio at point P_i
θ_{P_i}	Estimator variables for point P_i
e_{P_i}	Error of estimator variables for point P_i
Γ_{P_i}	Growth rate of the estimator for P_i
$\hat{\Pi}$	Matrix of all estimating unknown stiffness ratio
Ψ	Constant matrix
Φ	Matrix of all growth rate values
E	Matrix of all error of estimator variables
Θ	Matrix of all estimator variables
$\hat{G}$	Matrix form of the estimated stiffness ratio
	Correspondence selection and implementation via the estimator
l	Index of updating the estimated stiffness ratio
$r_{\hat{g}}(P_i)$	A time-varying weight
h_{D_i}	A N by 1 matrix, including closest distance of points from $\mathcal{T}$ to P_i
h_{K_i}	A N by 1 matrix, including closest shape descriptor value of points from $\mathcal{T}$ to P_i
H_D	A matrix including h_{D_i}
H_K	A matrix including h_{K_i}
	The simulation configuration
$\hat{g}^{\max}$	Maximum stiffness
$\hat{g}^{\min}(k)$	Stiffness trade-off
N_{mean}	Target points averaging size
N_r	Initial ratio of n points on $\mathcal{S}$
$N(k)$	Target points pool size
ϵ	Convergence error threshold
$j^{\max}$	Convergence iteration threshold
$k^{\max}$	Number of iteration for the outer loop

Regarding the figure, triangular meshes are used, and the vertices are indexed by numbers. In the step, first, the correspondences from vertices v_{P_i} in the source surface $\mathcal{S}$ (red) to vertices u_{P_i} in the target surface $\mathcal{T}$ (gray) are selected. Then v_{P_i} is transformed via locally affine transformation (X_{P_i}) towards the target surface $\mathcal{T}$. Here, the transformation matrix X_{P_i} for each vertex in the source mesh is a 3×4 transformation matrix which includes all possible translation and rotation transformations. Thus, the transformation matrix X of all vertices is defined in a

$4n \times 3$ matrix as $X = [X_{P_1} \cdots X_{P_n}]^T$. The transformed source surface is $\mathcal{S}(X)$. This procedure iterates until an optimum state is achieved.

Here, according to a defined correspondence set, namely (v_{P_i}, u_{P_i}), a cost function based on Amberg [45] is determined. Accordingly, Amberg [45] proposed the non-rigid registration formulation as a combination of distance and stiffness terms summarised in the following formula

$$\bar{J}(X) = \left\| \begin{bmatrix} M \otimes G \\ WD \end{bmatrix} X - \begin{bmatrix} 0 \\ W\tilde{U} \end{bmatrix} \right\|_F^2 \tag{1}$$

where the sparse matrix D is formed to facilitate the transformation of the source points with the individual transformations in X through matrix multiplication and defined as $D = \mathrm{diag}(v_{P_1}^T, v_{P_2}^T, \ldots, v_{P_n}^T)$. W is a diagonal matrix composed of weights w_i. In addition, $\tilde{U} \subset U$ includes the corresponding points from $\mathcal{S}$ to $\mathcal{T}$ which is a $n \times 3$ matrix, where $U = [u_{P_1}, u_{P_2}, \ldots, u_{P_n}]^T$. To regularise the deformation, an extra stiffness term is utilized. Employing the Frobenius norm $\|.\|_F$, the stiffness term minimizes differences in the transformations of adjacent vertices, via a weighting matrix $G = \mathrm{diag}(1, 1, 1, \gamma)$. In the deformation process, γ contains a value to stress changes in the skew and rotational part against the translation part of the deformation. The value of γ can be determined according to data units and the types of deformation [34]. The node-arc incidence matrix M (e.g. Dekker [46]) of the source mesh topology is used to turn the stiffness term functional into a matrix form. As the matrix is unchangeable for directed graphs, the construction is one row for each edge of the mesh and one column per vertex. To define the node-arc incidence matrix of the source topology, the indices (i.e. the subscripts) of edges and vertices are addressed. For any edge of r which is linked to vertices (i, j), in r^{th} row of M, the nonzero entries are $M_{ri} = -1$ and $M_{rj} = 1$.

C. Adaptive Estimator Design

A key objective in this research is to estimate and reconstruct a weighting matrix including ratios known as stiffness ratio ($\hat{g}_{P_i}$) per vertex P_i on $\mathcal{S}$, comprising G in (1). For this, we will define an Ordinary Differential Equation (ODE) based on the shape descriptor and the average of mesh quality where $\hat{g}_{P_i}$ will be its solution. To integrate the estimated $\hat{g}$ in the stiffness term in (1), we define the ratio in the form of a matrix as:

$$\hat{G}_{4n \times 4n} = \mathrm{diag}(\hat{g}_{P_i} I_{4\times 4}, \ldots, \hat{g}_{P_n} I_{4\times 4}) \tag{2}$$

which is embedded in the stiffness term

$$J_s = \|(M \otimes G)\,\hat{G}X\|_F^2. \tag{3}$$

Thus (1) is changed to:

$$J(X) = \left\| \begin{bmatrix} (M \otimes G)\hat{G} \\ WD \end{bmatrix} X - \begin{bmatrix} 0 \\ W\tilde{U} \end{bmatrix} \right\|_F^2 = \|\; AX - B \;\|_F^2, \tag{4}$$

The non-rigid registration can be achieved by optimizing the cost function in (4).

In this section, we first introduce the preliminary including the derivation of the ODE, the assumptions, the error system definition, and its stability and convergence in Section III-C1. In Section III-C2, we present the process of deriving the rules for estimating $\hat{g}_{P_i}$ using control theory that guarantees the asymptotic stability of the error system. In Section III-C3, we discuss the properties of estimation rules, and finally, we integrate the estimation rules into the non-rigid ICP scheme as Section III-C4.

1) Preliminary: For formulating the estimator states per vertex, we use the integral error states [47], [48] for (5), as they are robust to uncertainty and are able to accommodate for zero error convergence [49]

$$e_s = \int_0^t k_s^t - k_s^0 \, d\tau, \;\; e_q = \int_0^t q^t - q^0 \, d\tau, \tag{5}$$

where k_s^t and q^t are the shape descriptor value and the average of mesh quality value of the faces incident to an arbitrary vertex P_i on the source at time t, respectively. Accordingly, k_s^0 and q^0 are the values before registration, i.e. at time 0. Among different algorithms, Joe-Liu's parameter method [50] is used to juxtapose mesh quality in this paper. The method determines the quality value per vertex which varies in a range from 0 to 1, where 1 defines the highest quality and zero the lowest quality. Following (5), the integral error system is considered as

$$\dot{e}_s = k_s^t - k_s^0, \;\; \dot{e}_q = q^t - q^0, \tag{6}$$

To make the error system stable, we assume $\dot{e} = B_e u_e$, where $e = [e_s \; e_q]^T$ and u_e is the control input, and using (6) we will have

$$\dot{x} = B_e u_e + r_e, \tag{7}$$

where

$$x = \begin{bmatrix} \int k_s^t \, dt \\ \int q^t \, dt \end{bmatrix}, B_e = \begin{bmatrix} 1 & 0 \\ 0 & 1 \end{bmatrix}, r_e = \begin{bmatrix} k_s^0 \\ q^0 \end{bmatrix}, \tag{8}$$

and u_e as the control input is a 2×1 matrix that should be designed to guarantee the stability of (7). To this end, we aim at controlling the state-space (7) through Model Reference Adaptive Control (MRAC) [24], which leads to penalisation of the tracking error. Accordingly, we assume a Proportional-action (P-action) feedback control law (see e.g., chapter 1 in [51]) that tries to penalise the error of tracking between the variable x, and the desired variables r_e with unknown gains as

$$\begin{aligned} u_e &= -\hat{g}_{P_i}(x - r_e) \\ &= -\hat{g}_{P_i} x + \hat{g}_{P_i} r_e, \end{aligned} \tag{9}$$

where $\hat{g}_{P_i}$ is an unknown scalar of the stiffness ratio for the point P_i that needs to be estimated. By assuming $\tilde{a} = \hat{g}_{P_i}\bar{I}$ and $\bar{I}_{2\times 4} = [-I \quad I]$, where I is an identity matrix with size 2×2, then,

$$u_e = \tilde{a} \begin{bmatrix} x \\ r_e \end{bmatrix}. \tag{10}$$

A model reference state is considered as

$$\dot{x}_M = -A_M x_M + B_M r_e, \tag{11}$$

where the optional predefined matrices A_M and B_M are used to establish a stable model reference in each iteration. Accordingly, the error is considered as the differences between the integral states (x), and the model reference states (x_M), where

$$\begin{aligned}\dot{e}_{P_i} &= \dot{x} - \dot{x}_M\\ &= B_e(-\hat{g}_{P_i}x + \hat{g}_{P_i}r_e) + r_e + A_M x_M - B_M r_e + A_M x - A_M x\\ &= -A_M(x - x_M) + B_e\left(-\hat{g}_{P_i}I + \frac{A_M}{B_e}\right)x\\ &\quad + B_e\left(\hat{g}_{P_i}I - \frac{B_M + I}{B_e}\right)r_e\\ &= -A_M e_{P_i} + B_e\left(-\hat{g}_{P_i}I + \frac{A_M}{B_e}\right)x\\ &\quad + B_e\left(\hat{g}_{P_i}I - \frac{B_M + I}{B_e}\right)r_e. \end{aligned} \tag{12}$$

This results in the following error dynamic system equation explained in Laplacian domain.

$$e_{P_i} = \frac{B_e}{sI + A_M}\left[-\hat{g}_{P_i}I + \tfrac{A_M}{B_e} \qquad \hat{g}_{P_i}I - \tfrac{B_M + I}{B_e}\right]\begin{bmatrix} x \\ r_e \end{bmatrix}, \tag{13}$$

where s is the Laplace variable. As A_M can be selected to guarantee that the reference model becomes stable inherently i.e., $-A_M$ has negative eigenvalues therefore $(sI + A_M)$ is stable, the error dynamic of (13) is, then, stable in domain of time, if $\tilde{a}$ is bounded (or $\tilde{a}$ is converging).

2) Derivation of the Estimation Rule: Accordingly, to demonstrate that the $\tilde{a}$ is converging in the integral error dynamic in (13), a Lyapunov function for each of the vertex P_i is employed as follows:

$$\mathcal{V} = x\mathcal{P}x^T + \tilde{a}\Gamma_{P_i}^{-1}\tilde{a}^T, \tag{14}$$

where $\mathcal{P} \geq 0$ and $\Gamma_{P_i} > 0$ imply that $\mathcal{V} > 0$. Then, to prove the stability it would be sufficient to prove that $\dot{\mathcal{V}} \leq 0$ [52]. As

$$\frac{d\mathcal{V}}{dt} = \dot{x}^T\mathcal{P}x + x^T\mathcal{P}\dot{x} + \dot{\tilde{a}}^T\Gamma_{P_i}^{-1}\tilde{a} + \tilde{a}^T\Gamma_{P_i}^{-1}\dot{\tilde{a}}. \tag{15}$$

Based on (10) and considering $\theta_{P_i} = \begin{bmatrix} x \\ r_e \end{bmatrix}$, then $u_e^T = \theta_{P_i}^T\ \tilde{a}^T$, thus

$$\frac{d\mathcal{V}}{dt} = 2\mathcal{P}B_e x\theta_{P_i}^T\tilde{a}^T + 2\dot{\tilde{a}}\Gamma_{P_i}^{-1}\tilde{a}^T. \tag{16}$$

Following the assumption $\mathcal{P}B_e = c, e_{P_i} = cx$, and $\frac{d\mathcal{V}}{dt} = 0$, then from (16) we obtain

$$-2\ e_{P_i}\theta_{P_i}^T\tilde{a}^T = 2\dot{\tilde{a}}\Gamma_{P_i}^{-1}\tilde{a}^T; \tag{17}$$

Accordingly, to meet the stability criterion, the variation of $\tilde{a}$ by the time must follow the estimation rule as

$$\dot{\tilde{a}} = -\ e_{P_i}\ \ \theta_{P_i}^T\ \ \Gamma_{P_i}, \tag{18}$$

where Γ_{P_i} is the growth rate of the estimation rule. To define the estimation rule for $\hat{g}_{P_i}$, by multiplying $\bar{I}^T$ to both sides of (18), and knowing that $\bar{I}\bar{I}^T = 2I$ and $\tilde{a} = \hat{g}_{P_i}\bar{I}$, we will have

$$\dot{\hat{g}}_{P_i}I = -0.5\ \ e_{P_{i_{2\times 1}}}\ \ \theta_{P_{i_{4\times 1}}}^T\ \ \Gamma_{P_{i\,4\times 4}}\ \ \bar{I}_{2\times 4}^T \tag{19}$$

To extend (19) to all vertices of the source mesh, we consider the matrix form as

$$\dot{\hat{\Pi}}_{2n\times 2n} = -0.5\ \ E_{2n\times n}\ \ \Theta_{4n\times n}^T\ \ \Phi_{4n\times 4n}\ \ \Psi_{4n\times 2n}, \tag{20}$$

where Φ is a diagonal matrix composed of each Γ_{P_i} as $\Phi = \text{diag}(\Gamma_{P_1}, \Gamma_{P_2}, \ldots, \Gamma_{P_n})$. Ψ is a diagonal matrix where each component on the diagonal of the matrix is $\bar{I}^T$. In addition, E is a diagonal matrix composed of each e_{P_i} as $E = \text{diag}(e_{P_1}, e_{P_2}, \ldots, e_{P_n})$ and Θ is a diagonal matrix composed of each θ_{P_i} as $\Theta = \text{diag}(\theta_{P_1}, \theta_{P_2}, \ldots, \theta_{P_n})$. As a result, $\dot{\hat{\Pi}}$ is a diagonal matrix composed of each $\dot{\hat{g}}_{P_i}$ as $\dot{\hat{\Pi}} = \text{diag}(\dot{\hat{g}}_{P_1}I, \dot{\hat{g}}_{P_2}I, \ldots, \dot{\hat{g}}_{P_n}I)$.

3) The Growth Rate (Γ_{P_i}) Design: To simplify the (19), we design $\Gamma_{P_i} = \bar{\Gamma}_{P_i}I_{4\times 4}$, where $\bar{\Gamma}_{P_i}$ is a scalar. Empirical observations indicate that under condition of $|\dot{\hat{g}}_{P_i}| > 1$, high fluctuations in the estimation of $\hat{g}_{P_i}$ values are expected, which may lead to a decrease in the convergence level of the estimator. To prevent this, $\bar{\Gamma}_{P_i}$ is formulated in the form below to guarantee $\bar{\Gamma}_{P_i} \leq 1$ for a smoother converging towards the true values.

$$\bar{\Gamma}_{P_i} = \begin{cases} \frac{1}{|\dot{\hat{g}}_{P_i}|^{\zeta}}, & \text{if } |\dot{\hat{g}}_{P_i}| > 1,\\ |\dot{\hat{g}}_{P_i}|^{\nu}, & \text{if } |\dot{\hat{g}}_{P_i}| \leq 1. \end{cases} \tag{21}$$

Discussion I: In (21), ζ and ν are very effectual on the changes of $\bar{\Gamma}_{P_i}$ by the time. And large values of $\bar{\Gamma}_{P_i}$ can lead the system to an unstable condition as the system and control scheme are very dependent on the estimated stiffness ratio. Thus, $\bar{\Gamma}_{P_i}$ should be chosen so that the estimator is fast enough with the least overshoot. For the possible domain of ζ and ν, we list four conditions as follows.

1) *$\zeta < 0$ and $\nu < 0$:* This condition is unstable as $\bar{\Gamma}_{P_i}$ would be greater than 1 especially when $\dot{\hat{g}}_{P_i} \to 0$ results in $\bar{\Gamma}_{P_i} \to \infty$.
2) *$\zeta < 0$ and $\nu > 0$:* In this condition, for some cases where $|\dot{\hat{g}}_{P_i}| > 1$, $\bar{\Gamma}_{P_i}$ would be comparatively a large value, which increases the chance of having overshoots.
3) *$\zeta \geq 0$ and $\nu \geq 0$:* Only here, some stable points may be found via numerical trial and error methods as in this condition $\bar{\Gamma}_{P_i}$ is bounded ($\bar{\Gamma}_{P_i} \leq 1$).
4) *$\zeta > 0$ and $\nu < 0$:* Here and similar to condition 1, for $|\dot{\hat{g}}_{P_i}| < 1$, $\bar{\Gamma}_{P_i}$ has a large value which increases the probability of instability more than the condition 2.

In this research, condition 3 is selected for the possibility to guarantee the stability of the system. The ranges of ζ and ν will be studied in Section IV-D.

4) The Estimator Framework: The estimator framework presented in this paper, shown in Fig. 3, includes an estimator for each point P_i on $\mathcal{S}$ to predict the unknown stiffness ratio $\hat{g}_{P_i}$ during the registration process. It is expected that such a design can balance the two competing factors, shape deformation and feature preservation (k_s^t and q^t), in the non-rigid registration process.

The estimator framework is composed of two main parts: a) adaptive growth rate estimation (dark blue part), and b) the adaptive estimator (medium blue part). The dark blue part essentially defines a conservative time-varying growth rate ($\bar{\Gamma}_{P_i}$) value in (21) used in forming matrix Γ_{P_i} employed in the estimation rule

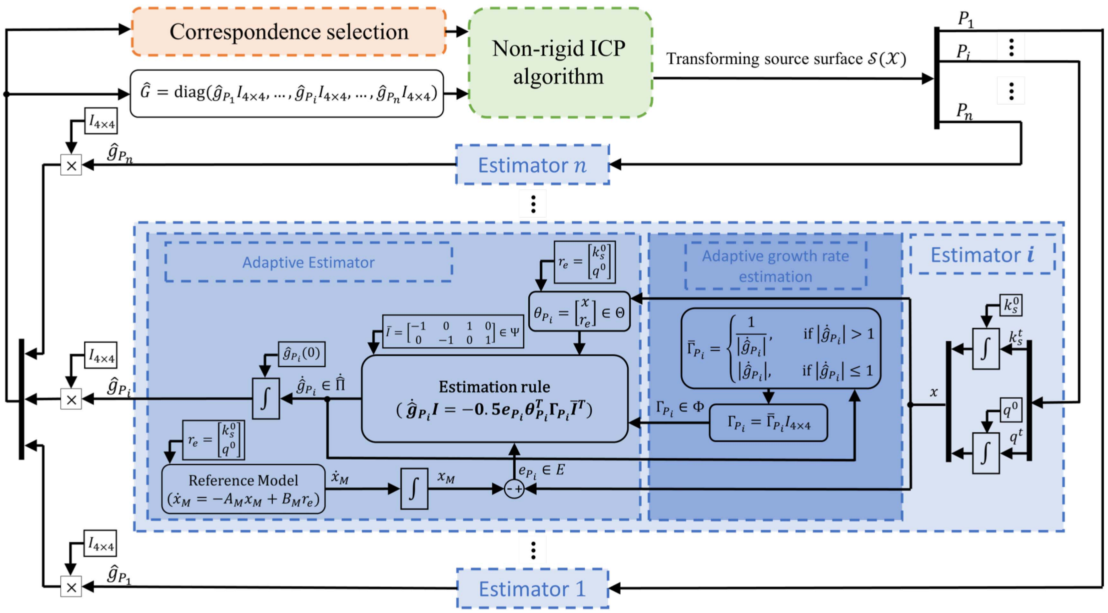

Fig. 3. Closed-loop diagram of the proposed estimation and registration method integration framework.

(19). The medium blue part represents the estimation process of $\hat{g}_{P_i}$ which is the output of the estimator. The set of all $\hat{g}_{P_i}$ is then used in the correspondence selection (orange part) directly, and in the non-rigid ICP cost function (green part) via $\hat{G}$ in (4).

D. *Correspondence Selection and Implementation Via the Estimator*

The flowchart in Fig. 4 presents more details of the presented process for obtaining the optimal X_{P_i} from v_{P_i} to u_{P_i} (where u_{P_i} is comparable with $X_{P_i} v_{P_i}$) in each iteration. In Fig. 4, two nested loops are embedded: regarding the outer loop (where k is updated, counts the outer loop iterations), the weighting parameters related to the correspondence selection scheme are automatically updated; for the inner loop (where j is updated), the cost function for obtaining the optimal transformation matrix is incessantly being minimized according to the weights until the variation of the last two consequential Xs is less than a small value of ϵ or $j > j^{\max}$. As the $\hat{g}$ is never reset after each update in k, it is updated with index $l = (k-1)j^{\max} + j$. The nested loops in each of their iterations aim at referring various aspects of the measures, e.g. the euclidean distance and the difference of curvature values of two corresponding points are affected by the estimated stiffness ratio $\hat{g}$.

1) Establish Correspondences: In the context of establishing correspondences in an ordinary ICP method, the corresponding point for a vertex on $\mathcal{S}$ is the closest vertex on $\mathcal{T}$ if only the euclidean distance is considered as the only criterion, and the inherent properties of the mesh are not considered. To embed the inherent properties, a novel formulation as (22) is proposed balances distance and shape similarity using the estimated $\hat{g}_{P_i}$. The formulation integrates both the euclidean distance and the descriptor to determine the corresponding vertex on $\mathcal{T}$ as:

$$r_{\hat{g}}(P_i) = \frac{\hat{g}_{P_i} - \min(\hat{g})}{\max(\hat{g} - \min(\hat{g}))} \tag{22}$$

$$H = (1 - r_{\hat{g}})H_D + r_{\hat{g}} H_K. \tag{23}$$

Here, H_D belongs to the distance measures including h_{D_i} allied to P_i, and H_K belongs to the differential form of the shape descriptor term containing h_{K_i} allied to P_i. In addition, in (22), $r_{\hat{g}}(P_i)$ is a time-varying weight allied to P_i in the range of $[0,1]$ inspired by the corresponding estimated value of P_i as $\hat{g}_{P_i} \in \hat{g}$, e.g. it has a large value when the balance between the mesh quality and preserved shape descriptor value is low. Larger values of $\hat{g}$ define a higher stiffness requiring more convenient preservation of the features at the point location. The high values result in more emphasis on the shape descriptor term and vice versa. Practically, sparse similarities prohibit us to detect all points in $\mathcal{T}$ for establishing correspondences. Thus, only candidate correspondence points are used, considered in a pre-processed region containing N number of points in $\mathcal{T}$. Next, H_D and H_K in (23) can be elaborated as:

$$[h_{K_i}]_{N\times1} = \frac{\frac{k_s(P_i)}{\max(K_s)} - \frac{[K_T]_{N\times1}}{\max(K_T)}}{\max\left(\frac{k_s(P_i)}{\max(K_s)} - \frac{[K_T]_{N\times1}}{\max(K_T)}\right)} \tag{24}$$

$$[h_{D_i}]_{N\times1} = \frac{\mathrm{norm}\left(v_{P_i}^T - [\bar{U}]_{N\times3}\right)}{\max\left(\mathrm{norm}\left(v_{P_i}^T - [\bar{U}]_{N\times3}\right)\right)} \tag{25}$$

where K_T is composed of the shape descriptor values of the vertices on the $\mathcal{T}$, h_{D_i} is composed of a N by 1 matrix, including distances of the N vertices from $\mathcal{T}$ to P_i on $\mathcal{S}$ known as $\bar{U} \in U$. Likewise, h_{K_i} is composed of a N by 1 matrix, including divergence of the N vertices on $\mathcal{T}$ in terms of the shape descriptor

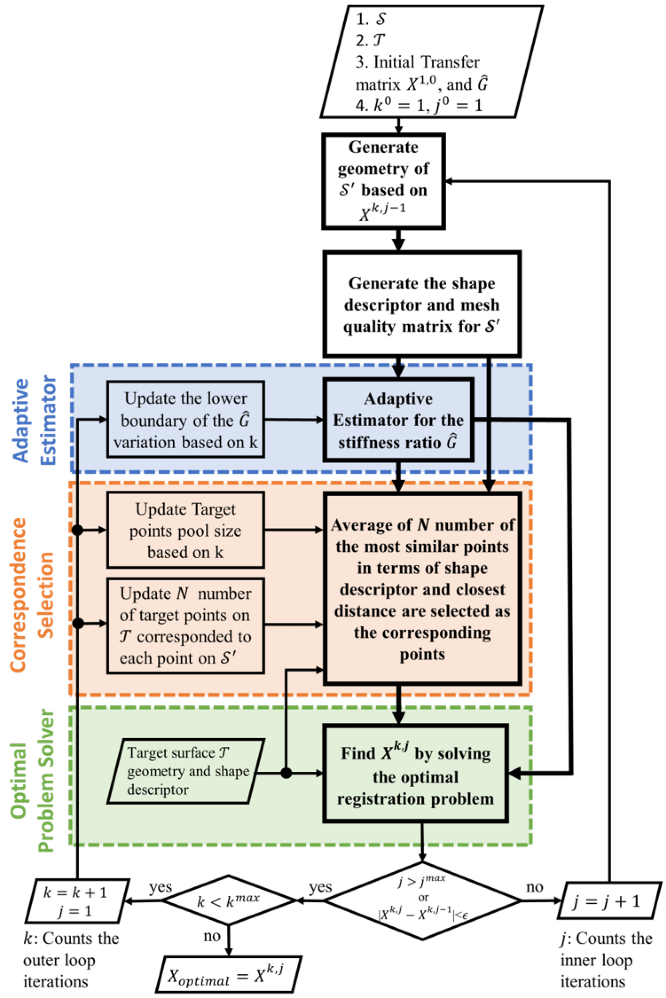

Fig. 4. The proposed registration process consists of two nested loops. In the outer loop (where k is updated), the weighting parameters related to the correspondence selection and the adaptive estimator schemes are automatically updated; for the inner loop (where j is updated), the stiffness ratios are estimated and then the cost function for obtaining the optimal transformation matrix is incessantly being minimized to finally find the best solution for $X_{optimal}$.

TABLE II
PARAMETERS USED IN SIMULATION CONFIGURATION

Parameter	$\hat{g}^{\max}$	$\hat{g}^{\min}(k)$	N_{mean}	N_r
Value	1000	$\hat{g}^{\max}$:1	3	0.1
Parameter	$N(k)$	ϵ	$j^{\max}$	$k^{\max}$
Value	$N_r n_{\mathcal{T}}$:N_{mean}	0.001	50	20

value from P_i on $\mathcal{S}$. The pre-processing strategy to detect the area with N_{mean} vertices follows two procedures:

- N (decreasing value), initiates from $N_r n_{\mathcal{T}}$ and ends with N_{mean} number of closest points on $\mathcal{T}$ to each point on $\mathcal{S}$ are selected, in which N_r represents a ratio with domain of $[0\ 1]$ and $n_{\mathcal{T}}$ defines the number of points on $\mathcal{T}$.
- N_{mean} number of the candidate vertices with a decreasing value of H are selected from the previous step where the corresponding point is the average of these N_{mean} vertices' geometry.

After the correspondence points are established from the $\mathcal{T}$, we investigate the number of corresponding points from the $\mathcal{S}$ to each of the points of the $\mathcal{T}$. For the vertices corresponding to more than N_{mean} number of source points, we only pick the N_{mean} of them with minimum H.

2) Discrete Time Implementation: In the implementation, we discretize the parameter estimation process by considering $\dot{\hat{\Pi}}(l) = \frac{\hat{\Pi}(l) - \hat{\Pi}(l-1)}{\Delta l}$; then, knowing that $\Delta l = 1$ as l is a sequentially increasing index, the estimation rule (20) turns into

$$\hat{\Pi}(l) = \hat{\Pi}(l-1) - 0.5\ E(l-1)\ \Theta(l-1)\ \Phi(l-1)\ \Psi. \quad (26)$$

Similarly, by considering $\dot{\hat{g}}_{P_i}(l) = \frac{\hat{g}_{P_i}(l) - \hat{g}_{P_i}(l-1)}{\Delta l}$, the discrete form of (21) will be

$$\bar{\Gamma}_{P_i}(l) = \begin{cases} \frac{1}{|\hat{g}_{P_i}(l) - \hat{g}_{P_i}(l-1)|^{\varsigma}}, & \text{if } |\hat{g}_{P_i}(l) - \hat{g}_{P_i}(l-1)| > 1, \\ |\hat{g}_{P_i}(l) - \hat{g}_{P_i}(l-1)|^{\nu}, & \text{if } |\hat{g}_{P_i}(l) - \hat{g}_{P_i}(l-1)| \leq 1. \end{cases} \quad (27)$$

IV. EXPERIMENT SETUP

A. Dataset

1) Main Dataset: Full Human Body: In the experiment, realistic 3D scans of the full human body, including holes and spikes, are chosen as geometric shapes for assessing the presented method, as the holes are always challenges for mesh quality preservation. The full human body scans are chosen among the Civilian American and European Surface Anthropometry Resource (CAESAR) dataset [53]. Here, we selected the first 101 scans from the Dutch population as the target mesh and assessed via the pre-selected LMs in each mesh. 74 landmarks are defined in [53] (from page 17 to page 30), while we employed 73 of them (LM74 on the butt block is neglected). Regarding the source mesh, we recruited the full body mesh included in the Wrap 3 software [54]. To unify the inputs, we remeshed the source mesh in [54] to the same number of vertices as the original source mesh.

2) Assessment Dataset: Thoracic Vertebra: To evaluate the performance of the proposed approach on more complicated freeform surfaces, the twelve thoracic vertebrae in a complete spine in [55] which is extracted from [56] are employed. All the surface meshes are re-meshed to 8000 vertices [57], resulting in uniform triangle surface meshes, to have a ground truth for comparing the mesh quality variation between different methods. In the dataset, thoracic vertebrae are mainly labelled by the prefix T and numbered 1 to 12 (e,g., $T7$ belongs to thoracic number 7). We selected $T7$ as the source surface and the rest of the eleven vertebrae as the target surfaces. 25 Landmark Points (LMPs) for a thoracic vertebra are defined in [58], while we employed 12 of the LMPs with index 2, 3, 4, 5, 10, 19, 20, 21, 22, 23, 24, and 25.

B. Parameters of the Proposed Method

Table II reports values of the parameters employed in the experiment which are listed in Table I. During the minimization of the cost function in (4), γ in G, was selected as 1. To avoid large changes in the value, we defined a time-varying bound for the parameter with a gradual relaxation saturation operator as:

$$\mathrm{sat}(\hat{g}_{P_i}(l)) = \begin{cases} \hat{g}^{\min}(k), & \text{if } \hat{g}_{P_i}(l) < \hat{g}^{\min}(k) \\ \hat{g}^{\max}, & \text{if } \hat{g}_{P_i}(l) > \hat{g}^{\max} \\ \hat{g}_{P_i}(l), & \text{otherwise,} \end{cases} \tag{28}$$

where $\hat{g}^{\min}(k)$ is the decreasing lower and $\hat{g}^{\max}$ is the constant upper bound for the input $\hat{g}_{P_i}(l)$. In the experiments $\hat{g}^{\max}$ is 1000 and $\hat{g}^{\min}$ is gradually decreased from 1000 to 1. This indicates that in this case, $\hat{g}^{\min}$ and $\hat{g}^{\max}$ were specified independent of the source mesh defined and only global deformations were allowed at the beginning of registration. In addition, the lower limit of the boundaries relies on the type of data [45]. Thus, a small value of $\hat{g}^{\max}$ may result in a singularity of A in (4), which falls into instability condition during solving the optimal problem. Consequently, our experiments began with a considerably high $\hat{g}^{\max}$. To maintain a smoother registration process, we used the mean of a number of points from a set with size of 3 ($N_{mean} = 3$). This N_{mean} number of points regarding H in (22). N number of points on $\mathcal{T}$, as an area to explore for the corresponding point to any vertices on $\mathcal{S}$, varied from 10 % of the total number of vertices in $\mathcal{T}$ to N_{mean}. In the implementation of [59], the system of linear equations that arises in each step was solved with the help of the UMFPACK library [60].

Discussion II: As we bound the variation of $\hat{g}$ in (28), it is expected that many iterations are needed to converge to the true stiffness ratio for some vertices. Necessity of the slow converging process is due to the fact that (1) is locally stable [45], and large over/undershoots of the $\hat{g}$ may cause the instability of (4). Thus, the initial guesses for the estimation process are key to accelerate the process of finding the true values in a limited number of iterations. In this paper, we use ANFIS method as a data-driven approach discussed in Section IV-E to predict the proper initial conditions for the estimator.

C. Reference Model Dynamics

Following the discussion presented in Section III, a stable reference model (A_{ref}, B_{ref}) must be established, in which two of the states are considered as the integral of the other two states. Accordingly, a four-state dynamic system is utilized as the reference model which its states (x_{ref}) are proposed below

$$\dot{x}_{ref} = A_{ref}x_{ref} + B_{ref}r_e \tag{29}$$

$$A_{ref} = \begin{bmatrix} 0 & 1 & 0 & 0 \\ -10 & -10 & 0 & 0 \\ 0 & 0 & 0 & 1 \\ 0 & 0 & -10 & -10 \end{bmatrix}, B_{ref} = \begin{bmatrix} 0 & 0 \\ 10 & 0 \\ 0 & 0 \\ 0 & 10 \end{bmatrix}, \tag{30}$$

where $x_M = [x_{ref_{1,1}} \; x_{ref_{3,1}}]^T$ in (11). The system is globally stable to r_e as all the eigenvalues of A_{ref} are negative, and pair (A_{ref}, B_{ref}) is stabilisable (see Chapter 2 of [61]), which can be verified through, e.g, the Hautus-test [62], [63]. Please note that, in this paper, for all the experiments that use the reference model we use the parameters in (30).

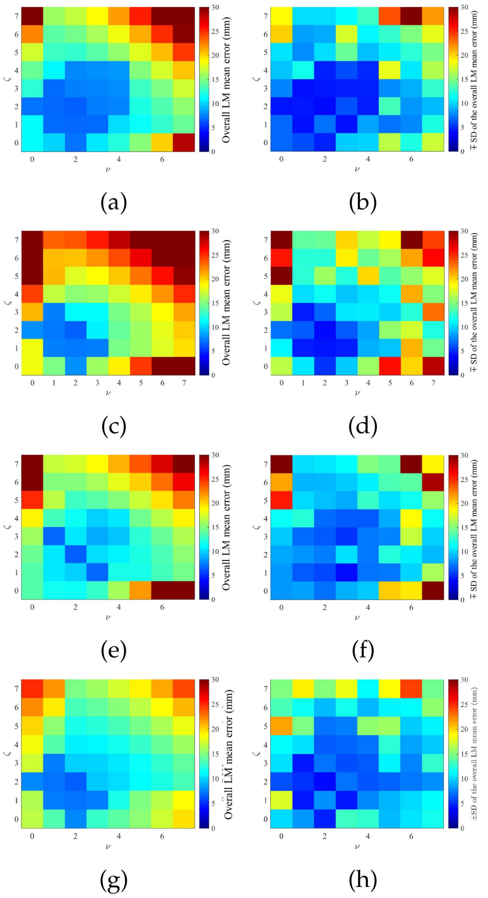

(a) (b)

(c) (d)

(e) (f)

(g) (h)

Fig. 5. Sensitivity analysis showing for a domain of ν and ζ while $N_r = 0.1$, (left) Overall LM mean error; (right) SD of Overall LM mean error based on: (a, b) MC formulation; (c, d) GC formulation; (e, f) SI formulation; (g, h) CI formulation.

D. Sensitivity Analysis Regarding Different Shape Descriptors

A set of experiments in the stable domain introduced in Discussion I are initially performed employing the scans from the Dutch population of the CAESAR dataset [53] to study the sensitivity of the parameters ν, and ζ per different shape descriptor aimed at selecting the proper range of the parameters and the descriptor. To this end, we select four shape descriptors (K_G) as Mean Curvature (MC), Gaussian Curvature (GC), Shape Index (SI), and Curvature Index (CI) from [64] with the following formulations:

$$\begin{cases} \mathrm{MC}: & \frac{\mu_1+\mu_2}{2}, \\ \mathrm{GC}: & \frac{\mu_1\,\mu_2}{2}, \\ \mathrm{SI}: & \frac{2}{\pi}\tan^{-1}\frac{\mu_2+\mu_1}{\mu_2-\mu_1}, \\ \mathrm{CI}: & \sqrt{\frac{\mu_1^2+\mu_2^2}{2}}, \end{cases} \tag{31}$$

where μ_1 and μ_2 are the principal curvatures at point P.

According to Fig. 5, which demonstrates how the achieved error and Standard Deviation (SD) of error vary by altering, in pairs, the weights employed in the $\bar{\Gamma}_{P_i}$ function (21), the algorithm is able to achieve a low error value (blue areas) for a wide range of those parameters regarding each of the descriptor. Looking at the Overall LM mean error of the figure, all the

TABLE III
AVERAGE RMSE AND R^2 RESULTS OF ANFIS PERFORMANCE FOR DIFFERENT MF TYPES VIA THE TEST DATA

MF type	psigmf	dsigmf	pimf	gaussm2f
RMSE	0.71	0.70	1.87	0.73
R^2	0.77	0.78	0.71	0.76
MF type	gaussmf	gbellmf	trapmf	trimf
RMSE	**0.69**	0.72	1.94	0.77
R^2	**0.89**	0.78	0.69	0.81

descriptors have stable performance around $\zeta = 2$, and $\nu = 2$ which is visible with blue region; however, the area of the region explains the degree of robustness is changing. The robustness is theoretically expected because the system is globally asymptotically stable as investigated in Section III, and here the expectation was proved as there was limited sensitivity regarding the choice of the range of parameters, and no fine-tuning is further needed to obtain the desirable results.

According to the figure, GC has the highest sensitivity as the color variation is the fastest and CI has the least sensitivity due to slow changes in the color. Meanwhile, MC has the biggest area with the least error (dark blue area), thus we choose MC formula for our calculation.

E. ANFIS Initial Condition Predictor

Following Discussion II, the main challenge of designing an ANFIS model is determining the proper inputs and output [65]. First, the stiffness ratio is estimated through Mean Curvature and mesh quality values (both explain the topology of the mesh) defined in Sections III and IV-D. Second, the distance between the point on $\mathcal{S}$ and its correspondence on $\mathcal{T}$ affects the level of stiffness i.e. when the distance is high, the stiffness should be high as well for being able to transfer the features and then register on the target. Thus, we consider the normalised distance (input 1) and the differences between the normalised the Mean Curvature (MC) values (input 2) of each point on the $\mathcal{S}$ and its correspondences on $\mathcal{T}$ before registering as the inputs of the ANFIS model. Consequently, we consider the initial stiffness ratio as the output of the model. We used the final results of the adaptive estimator in Fig. 5 regarding the MC formulation in (31) as the label of the model, where $\zeta = 2$, and $\nu = 2$ consists of 101 registered meshes.

We considered the source mesh before registration as $\mathcal{S}$ and the registered source mesh via the adaptive estimator as $\mathcal{T}$ to generate the inputs of the training data of the model and the final estimated ratios as the ANFIS outputs. Therefore, the dataset includes 101 scans, and each scan contains 19882 vertices. 70 scans (equal to 70% of the dataset) are used as the train dataset and 31 (equal to approximately 30% of the dataset) are employed as test dataset [66], [67].

Eight different membership functions (MF) mentioned in Table III and explained in [68] were examined in the ANFIS model. The Root Mean Square Error (RMSE) and the correlation coefficient (R^2) between the anticipated values (initial stiffness ratio) and the true training values were employed to assess the performance of each MF, according to the lowest modeling RMSE and highest correlation coefficient. The results of averaging the RMSE and accuracy are reported in Table III, where the experiments are based on ten runs over 500 training epochs with linear MF type for output, and three MFs for each input. Regarding the modeling results reported in Table III, between the examined MFs, gaussmf performs to the highest accuracy and the smallest RMSE. Guassmf employs the general form of a gaussian function.

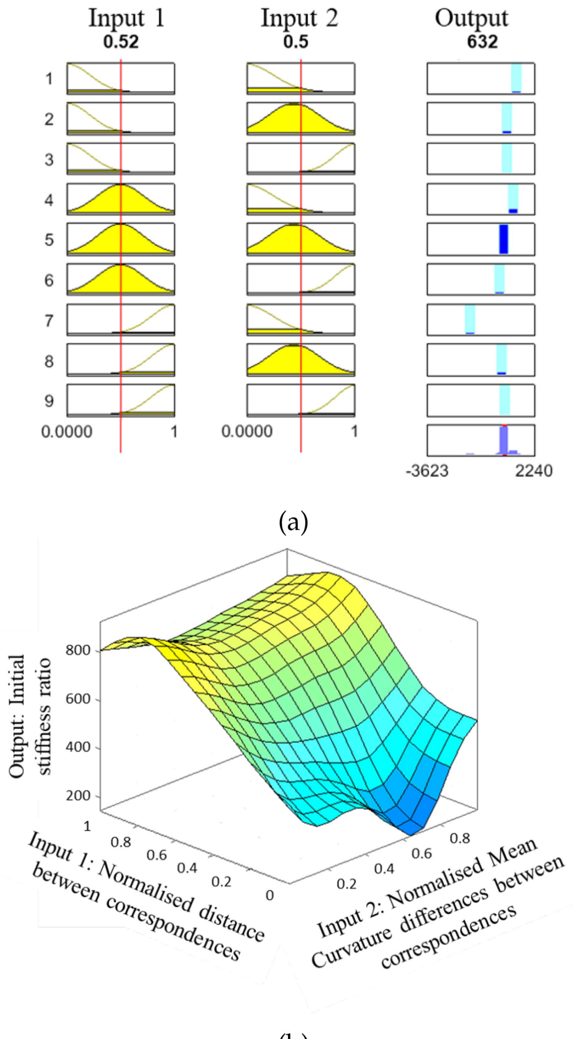

(a)

(b)

Fig. 6. ANFIS model. (a) Fuzzy rules. (b) Fuzzy surfaces for the intelligent estimator.

The ANFIS rules were selected to predict the proper initial stiffness ratio due to the normalized topology of $\mathcal{S}$ and estimated normalized travel distance that resulted in 9 fuzzy rules. Fig. 6(a) depicts these rules. To investigate the sensitivity of the model's inputs variation to its output variation, the level of prediction is shown in Fig. 6(b). According to the figure, the level of the model's inputs through its output shows a smooth area around the employed range of the output, and inputs reached steady, which conveys the acceptable level of design relationships, sensitivity, and robustness of the predictor output to its inputs.

F. Employed Methodologies for Comparison

For the experiment, the performance of the proposed approach is compared to several existing non-rigid registration methods presented by Amberg et al. [34], Andriy et al. [69], and Hirose [31], where the executable source code for each method is available in [59], [70], and [71] respectively, and Tajdari et al. [30].

Briefly, Amberg's method introduced an optimal step non-rigid ICP methodology utilising a variety of regularisations, while employing a range of lowering stiffness parameter equals for all the vertices.

Andriy account for the CPD algorithm [69] utilising Gaussian radial basis functions as a substitution for thin-plate splines which investigates another type of regularizer. Through the approach, the rigid and non-rigid registrations are considered, although the method is not optimal in identifying a large number of outliers and in establishing all the possible correspondences, which is generally identified as Non-deterministic Polynomial-time hard (NP-hard). The executable source code employed in this paper is achievable in [70].

Hirose proposed the BCPD method [31], using variational Bayesian inference theory to convey the coherent drift. The executable source code employed in this paper is achievable in [71].

Tajdari introduced a novel geometry feature as semi-curvature for better classification and corresponding point selection performance. Also, he linearized the term and integrated to the Amberg's solver and showed the linear version is globally stable; however, the method was ill to preserve the mesh quality for the boundary of missed parts, e.g. holes.

As both Amberg's method and Tajdari's method are using the same stiffness term integrated with the weighting matrix G same as (1), we are able to apply the estimator to both methods. We named these two variants as adaptive Amberg's method and adaptive Tajdari's method. Comparing our both proposed methods with the adaptive Amberg and the adaptive Tajdari may reveal the generalizability and extendability of our estimator for a variety of applications.

All methods were implemented by MatlabR2020a on a computing platform with an Intel Core-i5$^{\text{TM}}$ 9600 K 4.6 GHZ processor.

V. EXPERIMENT RESULTS

A. Effect of the Adaptive Scheme During Registration

Here, we study the impact of the adaptive controller on the level of feature preservation after registration, via a few experiments employing some basic shapes, in terms of quality of mesh and the degree of followed topology, especially for highly curved areas, missed areas, disconnected areas, and misaligned areas.

1) Feature Preservation: As we would like to investigate the impact of the estimator on the performance of the registration process only the methods with similar mechanisms are included.

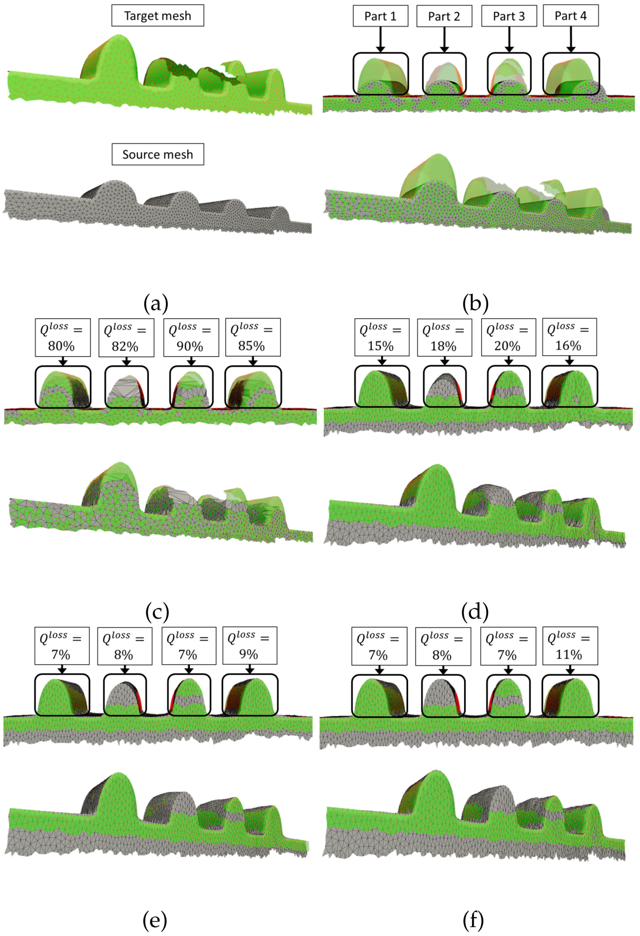

Fig. 7. Curved shape preservation experiment: Front view on top, and the perspective view on the bottom. (a) Target and source meshes (b) The initial condition (c) setup Registration using Amberg's method. (d) Registration using Tajdari's method method. (e) Our adaptive method. (f) Our ANFIS adaptive method.

To show the effect, a shape with three spherical cross-sections (gray) is used as $\mathcal{S}$ and a shape with three ellipsoidal cross-sections (green) is recruited as $\mathcal{T}$ depicted in Fig. 7(a). Fig. 7(b) shows the initial condition and the different regions for assessment as feature matching (part 1) to evaluate the accuracy of corresponding selection of points with similar normalized Mean curvature values, missed area (part 2), disconnected area (part 3), and misaligned part (part 4). We introduce a new measure named percent of mesh quality loss (Q^{loss}) for the evaluation as

$$Q^{loss} = 100 \times \left(1 - \frac{Q_S^{end}}{Q_S^0}\right) \tag{32}$$

where Q_S^0 and Q_S^{end} are the mesh quality of the source mesh for a region in the first and last intervals respectively. Fig. 7(c) presents the performance of Amberg's method in the four regions where it loses 80%, 82%, 90%, and 85% of mesh quality for part 1, part 2, part 3, and part 4 respectively. Fig. 7(d) figures the performance of Tajdari's method in the four regions with 15%, 18%, 20%, and 16% mesh quality loss for part 1, part 2, part 3, and part 4 respectively. Our adaptive method and our ANFIS adaptive method outputs are drawn in Fig. 7(e) and (f) which report the same performance in terms of mesh quality loss of 7%, 8%, and 7% for the first three regions. In addition, our adaptive method

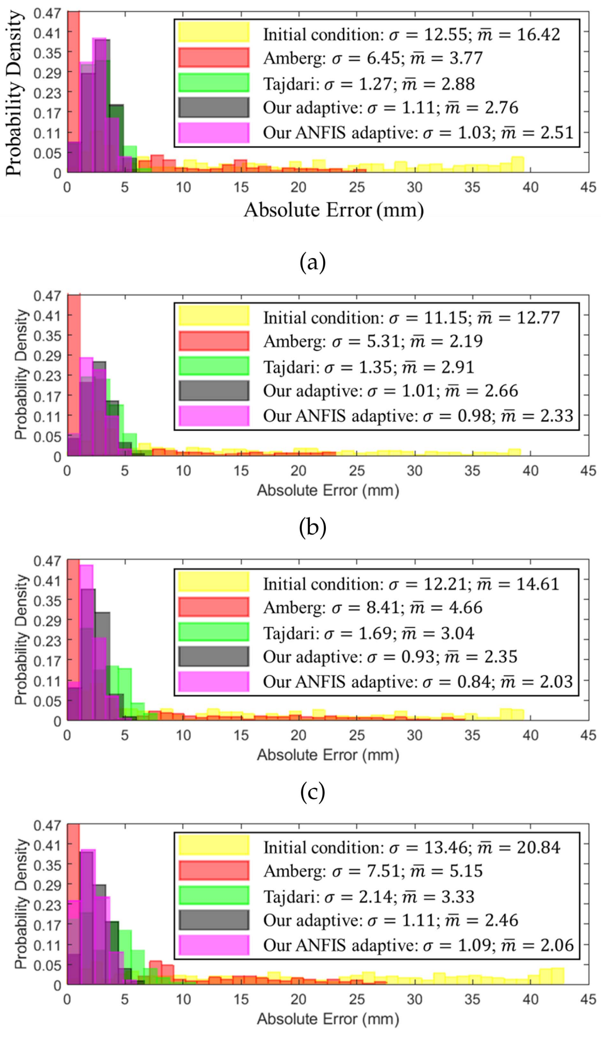

(a)

(b)

(c)

(d)

Fig. 8. Histogram graph of closest distance from target mesh points to source mesh points where the Diameter of the Bounding Box (DBB) is 691 (mm). (a) Part 1: feature matching. (b) Part 2: missed part. (c) Part 3: disconnected part. (d) Part 4: Misaligned part.

has 2% less mesh quality loss than our ANFIS adaptive method for the part 4.

2) Level of Convergence to the Target Mesh Topology: Preserving the mesh quality and following the topology of the target mesh during registration are competing with each other. As the mesh quality preservation needs more rigidity and following the topology requires less rigidity. To investigate the level numerically we figured the histogram graph, mean value ($\bar{m}$), and standard deviation (σ) of the closest distance population from target mesh points to source mesh points in Fig. 8 per part 1, part 2, part 3 and part 4, regarding each of the compared methods in Fig. 7. According to Fig. 8(a) where the part 1 is studied, Amberg's method has the highest σ, and our ANFIS adaptive method has the least σ. This shows our method could successfully reach the far points on the target mesh from the source mesh. However, as there is no missed area in the part 1, Tajdari's method has similar $\bar{m}$ and σ to our both methods.

Fig. 8(b) investigates the performance of the method in the presence of missed areas in the part 2. In this experiment, Amberg still has the highest $\bar{m}$ and σ values, while our both methods have better performance than Tajdari's method. Both of the proposed methods could follow the target mesh topology for about 28% better than Tajdari's method, which was expected due to better preservation of the source mesh feature close to the borders of the missed area.

In addition, Fig. 8(c) presents the results regarding the experiment of having disconnected areas as part 3. Although the conclusion for this part is similar to part 2, the advantage of our both methods is more visible here. Accordingly, our both methods outperformed for about 52% better than Tajdari's method in terms of $\bar{m}$, which shows the power of the adaptive estimator to face more borders of missed areas.

Furthermore, Fig. 8(d) may highlight more clearly the importance of the ANFIS predictor than the other experiments. As the ANFIS adaptive method has 13% and 16% less $\bar{m}$ compared to the adaptive method for the part 3 and part 4 experiments respectively. This shows the ANFIS adaptive method has 23% improvement based on the adaptive method, which resulted from more chance of freedom by having logically lower stiffness values in the initial condition of the registration process for the ANFIS adaptive scheme.

Overall, comparing Fig. 8(a), (b), (c), and (d) shows our ANFIS adaptive method has slightly better performance than our adaptive method in terms of $\bar{m}$ and σ values, this is because the ANFIS predictor is employed to avoid the stiffness ratio saturation meaning more flexibility for correct deformation of each point on the source mesh to follow the topology of the target mesh as rigid as possible. This is numerically investigatable by comparing Fig. 8(a), (b), (c), and (d), where the ANFIS adaptive method has on average 6% and 13% less value of the σ and $\bar{m}$ than the adaptive method respectively.

Discussion III: Using gradually decreasing uniform stiffness level for all the points in each interval of the registration process used in Amberg et al. [34], and Tajdari et al. [30] may cause mesh quality loss by converging several points on $\mathcal{S}$ to one point on $\mathcal{T}$. The mesh quality loss especially happens in the final intervals of the registration process where the stiffness term is sufficiently low then the surface can be deformed unfavorably and the source face features can be lost. Although Tajdari's method could partly solve the challenge by improving the accuracy of corresponding selection and avoiding the confliction contrary to Amberg's method, Tajdari's method was ill to preserve the features and mesh quality of the source mesh on the boundaries of missed areas and disconnected areas.

B. Full Human Body

In terms of validation, we use the CAESAR test dataset in Section IV-E and the predefined landmarks introduced in Section IV-A. Visually, the initial condition and the selected landmarks are shown in Fig. 9 for both the target and source meshes. The CEASAR dataset is suitable for assessment, as they are natural scans with holes, missed parts and natural noise e.g., a few examples are visually highlighted in Fig. 9(a). In terms

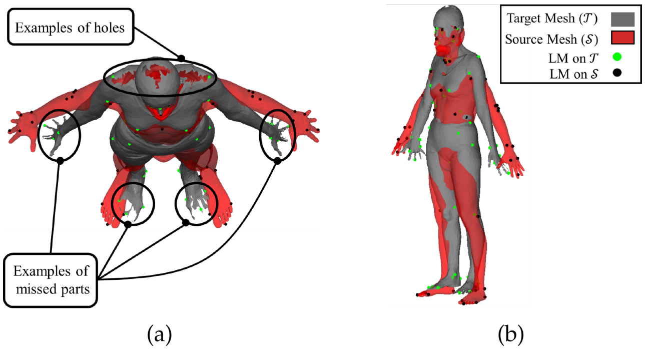

Fig. 9. Full body initial condition for one example among the test dataset. (a) Top-view. (b) Perspective view.

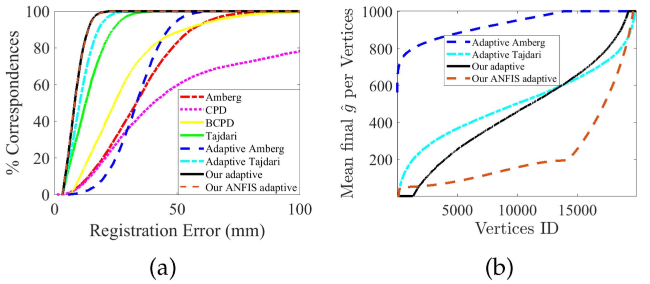

Fig. 10. Registration results via the test dataset for the case with 100% of the total vertices of the original source mesh. (a) Percentage correspondences according to registration error. (b) Sorted mean estimated stiffens ($\hat{g}$) per each vertex.

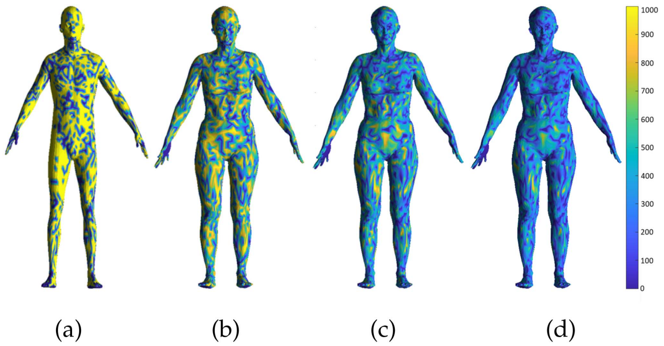

Fig. 11. Estimated final stiffness ratio color map. (a) Adaptive Amberg. (b) Adaptive Tajdari. (c) Our adaptive method. (d) Our ANFIS adaptive method.

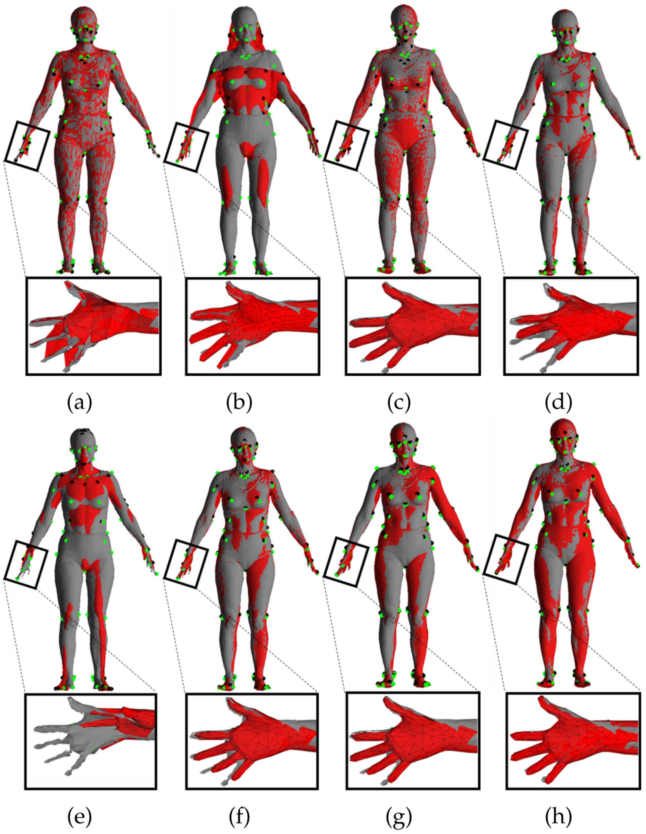

Fig. 12. Geometry of the full body registration results. (a) Amberg. (b) CPD. (c) BCPD. (d) Tajdari (e) Adaptive Amberg. (f) Adaptive Tajdari. (g) Our adaptive method. (h) Our ANFIS adaptive method.

of validation, the registration results are reported employing the remeshed source mesh with 100%, 60%, and 20% of the total vertices of the original source mesh.

The experiment results of the registration are reported in detail in Table IV, shown in Fig. 12. Please note that for the experiments that the ANFIS predictor is employed, $\hat{g}^{\min}$ in Table II considered as constant and equal to 1.

1) Landmark Error: Based on the Table IV(a) where the length of the Diameter of the Bounding Box (DBB) for $\mathcal{S}$ for the source mesh is 2167.6 mm, our both methods indicate on average about 78%, 91%, 75%, 30%, 80%, and 15% less landmark errors comparing to the Amberg's method, CPD method, BCPD, Tajdari's method, Adaptive Amberg's method, and adaptive Tajdari's method respectively. Fig. 10(a) presents the percentage of correspondences for the case with 100% of the total vertices of the original source mesh including all 73 selected landmarks for all the 26 scans (y-axis) from the test data, that have less distance error than a threshold (x-axis) [72]. According to the figure, the proposed two methods (black and brown lines) find all the correspondences earlier than the other four methods, and the errors are less than 21 mm, while for Amberg (red line), CPD (purple line), and BCPD (yellow line), Tajdari (green line), adaptive Amberg (blue line), and adaptive Tajdari (cyan line), the errors are 91 mm, 371 mm, 98 mm, 40 mm, 66 mm, and 30 mm, respectively. The results prove that the presented two methods are more accurate and robust compared to other methods.

2) Mesh Quality and Q^{loss}: Based on Table IV(b), the observed mesh quality preservation improvement of the proposed two methods is on average about 48% better than Amberg's method, 12% than the CPD method, 9% than the BCPD method, 11% with Tajdari's method, 6% than the adaptive Amberg's method, and 2% with adaptive Tajdari's method.

Moreover, in terms of Q^{loss} (in Table IV(b)) for the proposed two methods, one can be observed that they have on average 3% the quality loss while it is 44% for Amberg's method, 12% for CPD method, 10% for BCPD method, 14% for Tajdari's method, 7% for adaptive Amberg's method, and 6% with adaptive Tajdari's method.

Fig. 10(b) presents the sorted mean final value of $\hat{g}$ per vertex on $\mathcal{S}$, it can be inferred that the adaptive method tried to exert

TABLE IV
RESULTS OF REGISTRATION REGARDING THE FULL HUMAN BODY DATASET

a) Overall LM mean error ± Standard Deviation (SD) (mm).

Total vertices %	Amberg [35]	CPD [70]	BCPD [32]	Tajdari [30]	Adaptive Amberg	Adaptive Tajdari	Our adaptive	Our ANFIS daptive
100	31.3±17.5	77.1±99.3	28.2±23.3	11.2±7.7	33.5±10.1	8.1±6.9	7.4±3.9	**7.2±4.2**
60	31.9±29.7	93.3±101	44.1±27.4	13.9±13.3	39.9±14.6	11±8.1	**10.2±5.6**	9.1±4.4
20	50.8±55.2	189.1±127.3	53.5±51.6	18.3±22.1	40.1±14.8	17.4±18.1	21.3±9.7	**16.8±7.5**

b) Mesh quality mean value ± Standard Deviation (SD); Percent of mesh quality loss mean value (Q^{loss}) % in Eq. (32).

Total vertices %	Original mesh (Q_S^0)	Amberg [35]	CPD [70]	BCPD [32]	Tajdari [30]	Adaptive Amberg	Adaptive Tajdari	Our adaptive	Our ANFIS daptive
100	0.80±0.15	0.53±0.24; 36	0.67±0.23; 16	0.69±0.27; 14	0.68±0.29; 15	0.71±0.3; 11	0.74±0.17; 7	**0.75±0.1; 6**	0.74±0.13; 7
60	0.72±0.20	0.40±0.27; 43	**0.71±0.22; 1**	0.71±0.20; 1	0.65±0.31; 11	0.68±0.11; 5	0.68±0.14; 5	0.70±0.16; 3	0.70±0.18; 3
20	0.70±0.22	0.30±0.40; 56	0.57±0.24; 21	0.58±0.33; 16	0.53±0.45; 27	0.66±0.17; 6	0.66±0.2; 6	**0.69±0.13; 1**	0.68±0.11; 3

c) The run time mean value ± Standard Deviation (SD) (s).

Total vertices %	Amberg [35]	CPD [70]	BCPD [32]	Tajdari [30]	Adaptive Amberg	Adaptive Tajdari	Our adaptive	Our ANFIS daptive
100	**18.3±1.2**	1571±831	755±383	21.3±2.4	18.5±1.2	21.9±2.5	18.4±0.9	18.4±0.9
60	**12.5±0.9**	851±738	456±344	19.6±1.5	12.5±1.0	19.7±1.5	12.6±0.9	12.8±0.9
20	**8.0±0.4**	491±357	302±277	15.2±0.6	8.0±0.7	15.3±0.8	8.2±0.8	8.3±1.8

d) Mean distance between each point on $\mathcal{T}$ to the its closest point on registered S ± SD (mm).

Total vertices %	Amberg [35]	CPD [70]	BCPD [32]	Tajdari [30]	Adaptive Amberg	Adaptive Tajdari	Our adaptive	Our ANFIS daptive
100	**3.7**±5.5	17.7±12.5	6.1±3.2	13.1±3.7	16.1±11.9	18.7±5.4	9.3±3.7	6.2±**3.1**
60	**3.8**±5.5	19.2±13.8	6.8±3.9	16.3±5.2	16.3±11.6	20.3±7.8	10.1±3.6	7.1±**3.0**
20	**3.6**±5.9	20.1±13.5	7.4±4.1	19.1±7.1	16.4±11.7	24.7±9.9	10.6±3.7	7.5±**3.3**

rigid registration on the Amberg's method as the correspondences are mainly selected incorrect, thus the mesh quality should be decreased (toward zero area faces). Accordingly, the estimated $\hat{g}$ is very high. Adaptive Tajdari, Our adaptive and ANFIS adaptive methods achieved way lower the estimated values than the Adaptive Amberg method, while still, the ratio for our adaptive method stays less than adaptive Tajdari for more vertices (for about 15000 vertices over 19882 vertices), which means the correspondences are selected more accurate thus less deformation and less mesh quality loss is needed. Although our ANFIS adaptive method presents the same high quality registration as our adaptive method, the estimated stiffness ratios are considerably lower, which gives the opportunity to follow the topology of the target more accurately. This also can be observed visually by comparing the shown examples in Figs. 11, and 12 for one example.

3) Run Time Discussion: The computing speed is also a criterion to assess the performance of each mentioned method. Table IV(c) presents the computation time of all methods. Comparing the proposed two methods against other methods, the computing time reduction is about 0% less than Amberg's method, 99% less than CPD method, 97% less than BCPD method, 15% less than Tajdari's method, 0% less than adaptive Amberg's method, and 15% less than adaptive Tajdari's method. The results show our both methods have acceptable performance in terms of computing time regarding Amberg's method, however, both of them present relatively higher quality of registration regarding landmark error and mesh quality preservation.

4) Target-Source Distance Distribution: Table IV(d) reports the mean distance of each point on the $\mathcal{T}$ and the closest point on the registered $\mathcal{S}$ along the test data. According to the table, Amberg shows the least sparsity and CPD shows the largest sparsity in terms of the closest point. This happens as Amberg did not embed sufficient terms to keep the original geometry of $\mathcal{S}$. In addition to the error comparison, our both methods perform with the least error of correspondences and highest level of the source mesh geometry preservation. While, our ANFIS adaptive method presents 34% less error than our adaptive method, which allows us to perform more logical registration resulting in better following the topology of the target with similar quality of LM errors and surface quality.

C. Thoracic Vertebra

Using the same method in the previous section, we register the thoracic vertebra of $T7$ with DBB of 42 (mm), from the dataset in Section IV-A2 on the thoracic vertebrae of $T1,\ldots,T12$ excluding $T7$ (eleven vertebrae in total) using the methods in Section IV-F.

In all eleven experiments, the initial conditions for the eight methods are the same. As an example, the initial condition of the $T7$, and the $T1$ is presented in Fig. 13. Please note that we manually made some artefacts in the target meshes shown in Fig. 13i.e., holes and disconnected parts, in order to investigate the challenges discussed in Section I. In addition, the dataset is supposed to be able to highlight the advantages and disadvantages of each method as the variation of the shape of the vertebra from $T1$ to $T12$ is comparatively high [73]; however, all the vertebrae monopolize all the features belonging to a thoracic vertebra. For the used dataset in Section IV-A2, the value of Cranial Endplate Depth (EPD), over spinous process length (SPL) introduced in [73] are varying from 0.68 to 2 which highlights the topology variation.

For the assessment, we used the 12 landmarks explained in Section IV-A2 and shown in Fig. 13 with black dots (for $\mathcal{S}$) and green dots (for $\mathcal{T}$).

The registration results of using the eight methods are visually compared in Fig. 14 through an example of registering the $T7$

TABLE V
RESULTS OF REGISTRATION REGARDING THE THORACIC VERTEBRA DATASET

Original mesh (Q_S^0)	Amberg [35]	CPD [70]	BCPD [32]	Tajdari [30]	Adaptive Amberg	Adaptive Tajdari	Our adaptive	Our ANFIS daptive
a) Overall LM mean error ± Standard Deviation (SD) (mm).								
–	5.9±4.1	4.3±3.6	2.9±3.2	1.7±1.1	6.1±4.9	1.6±1.1	0.8±0.9	**0.7±0.9**
b) Mesh quality mean value ± Standard Deviation (SD); Percent of mesh quality loss mean value (Q^{loss}) % in Eq. (32).								
0.84±0.11	0.44±0.29; 48	0.63±0.22; 25	0.68±0.19; 14	0.69±0.20; 18	**0.82±0.20; 2**	0.72±0.19; 14	0.79±0.12; 6	0.76±0.16; 9
c) The run time mean value ± Standard Deviation (SD) (s).								
–	**10.1±0.9**	691±328	369±252	16.1±1.7	10.5±1.1	16.3±2.2	11.3±1.0	11.8±1.1
d) Mean distance between each point on $\mathcal{T}'$ (without artifacts) to its closest point on registered S ± SD (mm).								
–	0.95±0.81	0.39±0.33	0.32±0.29	0.19±0.15	1.4±1.8	0.23±0.21	0.12±0.13	**0.10±0.09**

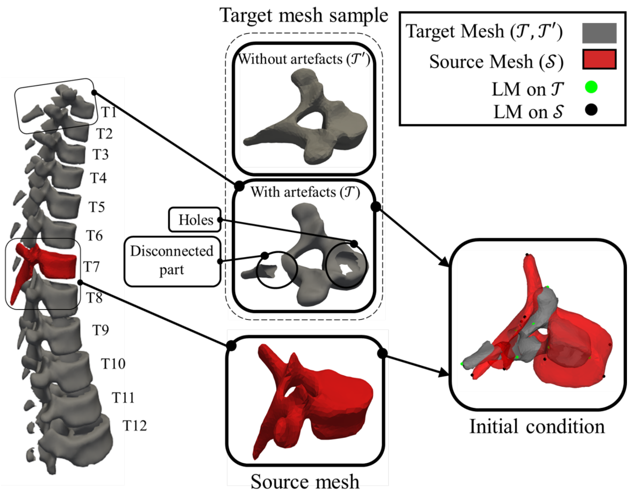

Fig. 13. The used thoracic dataset for assessment, including T1 as the target mesh, T7 as the source mesh, and their initial condition before non-rigid registration.

on the $T1$, and numerically investigated in Table V for all eleven registration results.

Errors between corresponding landmarks are reported in Table V(a) where our methods outperform Amberg's, CPD, BCPD, Tajdari's, adaptive Amberg's, and adaptive Tajdari's methods by an average of 87%, 82%, 74%, 56%, 87%, and 53% respectively regarding the mean absolute error. In addition, our ANFIS adaptive method presents 12% less error than our adaptive method.

Regarding the mesh quality of the source mesh after registration, Table V(b) shows that our methods present on average 7.5% the mesh quality loss, in which the value is about 48%, 25%, 14%, 18%, 2%, and 14% for Amberg's, CPD, BCPD, Tajdari's, adaptive Amberg's, and adaptive Tajdari's methods. According to the table, our methods have lower efficiency in terms of mesh quality only compared with adaptive Amberg's method, which comes from the fact that the adaptive solution found Amberg's algorithm path towards non-rigid registration, unfavorable and thus exerted as rigid as possible transformation. In other words, the adaptive Amberg's method presented high mesh quality as the registration was rigid mostly and thereby failed to match the target mesh. Furthermore, our ANFIS adaptive method presents 3% more mesh quality loss than our adaptive method.

In Table V(c), it can be found that using the CPD method is very time-consuming as the time duration for the experiment is about 6810%, 87%, 4191%, 6480%, 4139%, 6015%, and 5755% more than Amberg's, BCPD, Tajdari's, adaptive Amberg's, adaptive Tajdari's, our adaptive, and our ANFIS adaptive methods.

In Table V(d) contrary to the comparison using the full human body in Section V-B4, we compare the distance from the target meshes without the artefacts ($\mathcal{T}'$ in Fig. 13) to the registered source mesh for the eight methods. Note that this comparison was not possible for the full human body experiment as the original data of the CAESAR had the holes, missed parts, and natural noise. According to Table V(d), our methods outperform Amberg's, CPD, BCPD, Tajdari's, adaptive Amberg's, and adaptive Tajdari's methods by an average of 88%, 72%, 65%, 42%, 92%, and 52% respectively regarding the distance from the $\mathcal{T}'$ to the registered source mesh.

To have a holistic conclusion on the performance of the methods, we consider four matrices as $\mathcal{B}_i$ i.e., $i = 1, \ldots, 4$ where each of the matrices includes the mean values of the four features used in Table V. The mean value of each feature is named as $\mathcal{B}_i(z)$ i.e., $z = 1, \ldots, 8$ where z is corresponding to the number of the compared method, in the Table V with the same order of the methods. For example, $\mathcal{B}_3$ includes the mean run time values for all methods, where $\mathcal{B}_3(4) = 16.1$ (corresponded to Tajdari's method in Table V(c)). Note that from Table V(b), we only considered the percent of mesh quality loss mean value e.g, $\mathcal{B}_2(4) = 18$. Then, an energy function of J_z for each of the methods can be calculated as:

$$J_z(i) = \frac{\mathcal{B}_i(z)}{max(\mathcal{B}_i)} \tag{33}$$

The values of each J_z are drawn in Fig. 15, which shows that the overall performance by considering all matrices of comparison, our adaptive and ANFIS adaptive methods have the lowest value of the energy function which means the methods have the best performance. In addition, the median of the ANFIS adaptive method is slightly lower than our adaptive method, showing the positive impact of the ANFIS predictor on the overall performance of the method.

VI. LIMITATIONS

The presented methods address the feature preservation during a non-rigid registration via controlling the stiffness per vertex term in each iteration. Though using both methods can achieve higher quality of mesh and less landmark errors, they have several limitations. The source and target mesh should have

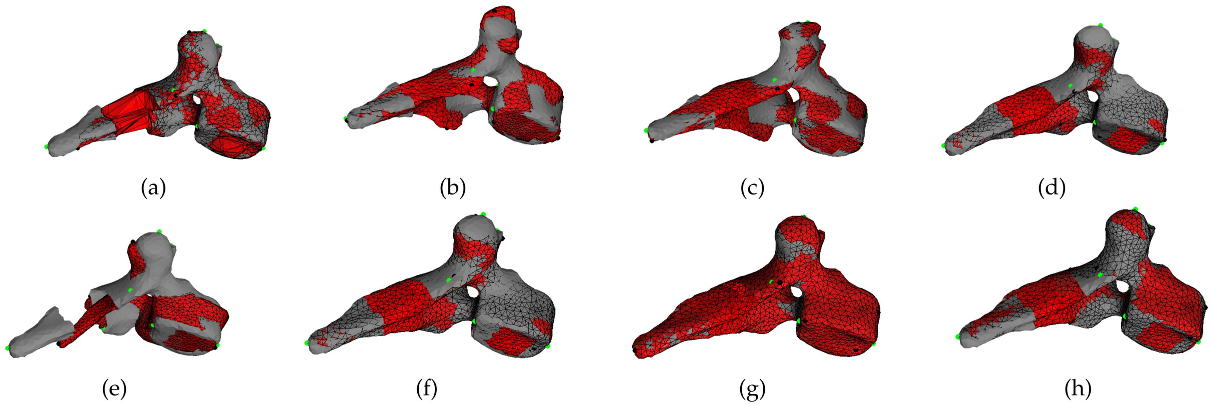

Fig. 14. Geometry of the thoracic vertebra registration results. (a) Amberg. (b) CPD. (c) BCPD. (d) Tajdari (e) Adaptive Amberg. (f) Adaptive Tajdari. (g) Our adaptive method. (h) Our ANFIS adaptive method.

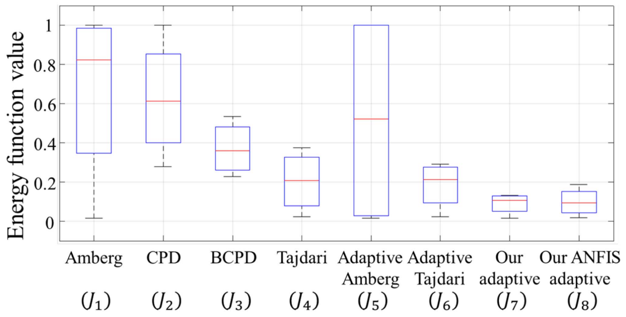

Fig. 15. Energy values box-plot per each method.

similar normalized curvature values for matching otherwise the adaptive estimator compels a rigid registration e.g., registering a human body on a dog body. This also prevents the method to tackle the challenges of high-frequency deforming objects e.g., a deforming cloth where the similar features of the target mesh to the source mesh are highly varying. Moreover, a weakness of using curvature values in establishing correspondences, is that the value is very sensitive to the noise, thus using mesh smoothing algorithms, e.g. Laplacian filter, is recommended prior to the registration. In addition, the global stability of (1) after integration of $\hat{G}$ in (4) is not investigated, as in Amberg [45], to prove the global stability of the solver.

VII. CONCLUSION

In this article, we introduce a non-rigid ICP approach integrated with a novel adaptive feedback control scheme to estimate the stiffness ratio utilizing the gradient of the mesh quality and Mean curvature values per vertex. To facilitate the convergence procedure of estimation towards the true values, an ANFIS-adaptive-based predictor is integrated with the estimator. The ANFIS predictor proceeds based on the topology of both the source and the target meshes to anticipate the initial values for the adaptive estimator to facilitate the procedure of the estimation. Then, we embedded the estimated ratio as part of the metric in establishing the correspondences and in the cost function, where the distance and the stiffness terms are integrated as well. Furthermore, by adjusting the connectivity level of vertices on their neighbors (equal to stiffness), the ANFIS based adaptive estimator elaborates on preserving the features of a surface in a globally asymptotically stable region during the process of registration, stressing mesh quality and convergence. Experimental outcomes show that the presented non-rigid method outperforms the aforementioned approaches, especially in the highly curved areas, missed areas, disconnected areas, and misaligned areas. This highlights the ability of the proposed method to employ the inherent characteristics of the complete surface during the process of registration.

REFERENCES

[1] K. Guo, F. Xu, T. Yu, X. Liu, Q. Dai, and Y. Liu, “Real-time geometry, albedo, and motion reconstruction using a single RGB-D camera,” *ACM Trans. Graph.*, vol. 36, no. 4, 2017, Art. no. 1.

[2] I. L. Dryden and K. V. Mardia, *Statistical Shape Analysis: With Applications in R*. Hoboken, NJ, USA: Wiley, 2016, vol. 995.

[3] J. Fan, X. Cao, P.-T. Yap, and D. Shen, “BIRNet: Brain image registration using dual-supervised fully convolutional networks,” *Med. Image Anal.*, vol. 54, pp. 193–206, 2019.

[4] M. Tajdari et al., “Next-generation prognosis framework for pediatric spinal deformities using bio-informed deep learning networks,” *Eng. Comput.*, vol. 38, no. 5, pp. 4061–4084, 2022.

[5] W. G. Aguilar, S. Morales, H. Ruiz, and V. Abad, “RRT* GL based optimal path planning for real-time navigation of UAVs,” in *Proc. Int. Work-Conf. Artif. Neural Netw.*, Springer, 2017, pp. 585–595.

[6] T. Heimann and H.-P. Meinzer, “Statistical shape models for 3D medical image segmentation: A review,” *Med. Image Anal.*, vol. 13, no. 4, pp. 543–563, 2009.

[7] A. L. Minnoye et al., “Personalized product design through digital fabrication,” in *Proc. Int. Des. Eng. Tech. Conf. Comput. Inf. Eng. Conf.*, 2022, Art. no. V002T02A054.

[8] W.-S. Lee and N. Magnenat-Thalmann, “Fast head modeling for animation,” *Image Vis. Comput.*, vol. 18, no. 4, pp. 355–364, 2000.

[9] S. Shirani, “Content-based multiple description image coding,” *IEEE Trans. Multimedia*, vol. 8, no. 2, pp. 411–419, Apr. 2006.

[10] D. Kim and D. Kim, “A fast ICP algorithm for 3-D human body motion tracking,” *IEEE Signal Process. Lett.*, vol. 17, no. 4, pp. 402–405, Apr. 2010.

[11] F. Tajdari, F. Kwa, C. Versteegh, T. Huysmans, and Y. Song, “Dynamic 3D mesh reconstruction based on nonrigid iterative closest-farthest points registration,” in *Proc. Int. Des. Eng. Tech. Conf. Comput. Inf. Eng. Conf.*, 2022, Art. no. V002T02A051.

[12] F. Tajdari, C. Eijck, F. Kwa, C. Versteegh, T. Huysmans, and Y. Song, “Optimal position of cameras design in a 4D foot scanner,” in *Proc. Int. Des. Eng. Tech. Conf. Comput. Inf. Eng. Conf.*, 2022, Art. no. V002T02A044.

[13] I. Toschi, E. Farella, M. Welponer, and F. Remondino, "Quality-based registration refinement of airborne LiDAR and photogrammetric point clouds," *ISPRS J. Photogrammetry Remote Sens.*, vol. 172, pp. 160–170, 2021.

[14] M. L. Tazir, T. Gokhool, P. Checchin, L. Malaterre, and L. Trassoudaine, "Cluster ICP: Towards sparse to dense registration," in *Proc. Int. Conf. Intell. Auton. Syst.*, Springer, 2018, pp. 730–747.

[15] K. Li, J. Yang, Y.-K. Lai, and D. Guo, "Robust non-rigid registration with reweighted position and transformation sparsity," *IEEE Trans. Vis. Comput. Graph.*, vol. 25, no. 6, pp. 2255–2269, Jun. 2019.

[16] R. Gal and D. Cohen-Or, "Salient geometric features for partial shape matching and similarity," *ACM Trans. Graph.*, vol. 25, no. 1, pp. 130–150, 2006.

[17] O. Oktay et al., "Stratified decision forests for accurate anatomical landmark localization in cardiac images," *IEEE Trans. Med. Imag.*, vol. 36, no. 1, pp. 332–342, Jan. 2017.

[18] T. Jiang, K. Qian, S. Liu, J. Wang, X. Yang, and J. Zhang, "Consistent as-similar-as-possible non-isometric surface registration," *Vis. Comput.*, vol. 33, no. 6/8, pp. 891–901, 2017.

[19] B. Ibragimov and T. Vrtovec, "Landmark-based statistical shape representations," in *Statistical Shape and Deformation Analysis*. New York, NY, USA: Academic Press, 2017, pp. 89–113.

[20] Y. Sahillioğlu, "Recent advances in shape correspondence," *Vis. Comput.*, vol. 36, no. 8, pp. 1705–1721, 2020.

[21] H. Dai, N. Pears, and W. Smith, "Non-rigid 3D shape registration using an adaptive template," in *Proc. Eur. Conf. Comput. Vis. Workshops*, 2018, pp. 48–63.

[22] L. Liang et al., "Nonrigid iterative closest points for registration of 3D biomedical surfaces," *Opt. Lasers Eng.*, vol. 100, pp. 141–154, 2018.

[23] C. Min, Y. Gu, Y. Li, and F. Yang, "Adaptive enhanced affine transformation for non-rigid registration of visible and infrared images," *IET Image Process.*, vol. 15, pp. 1144–1156, 2021.

[24] J.-J. E. Slotine et al., *Applied Nonlinear Control*, vol. 199. Englewood Cliffs, NJ, USA: Prentice Hall, 1991.

[25] H. Jin, Z. Liu, H. Zhang, Y. Liu, and J. Zhao, "A dynamic parameter identification method for flexible joints based on adaptive control," *IEEE/ASME Trans. Mechatron.*, vol. 23, no. 6, pp. 2896–2908, Dec. 2018.

[26] F. Tajdari, "Adaptive time-delay estimation and control of optimized Stewart robot," *J. Vib. Control*, 2022, Art. no. 10775463221137141.

[27] J. E. Gaudio, A. M. Annaswamy, E. Lavretsky, and M. Bolender, "Parameter estimation in adaptive control of time-varying systems under a range of excitation conditions," *IEEE Trans. Autom. Control*, vol. 67, no. 10, pp. 5440–5447, Oct. 2022.

[28] F. Tajdari and C. Roncoli, "Adaptive traffic control at motorway bottlenecks with time-varying fundamental diagram," *IFAC-PapersOnLine*, vol. 54, no. 2, pp. 271–277, 2021.

[29] S. Wang and J. Na, "Parameter estimation and adaptive control for servo mechanisms with friction compensation," *IEEE Trans. Ind. Informat.*, vol. 16, no. 11, pp. 6816–6825, Nov. 2020.

[30] F. Tajdari, T. Huysmans, Y. Yang, and Y. Song, "Feature preserving non-rigid iterative weighted closest point and semi-curvature registration," *IEEE Trans. Image Process.*, vol. 31, pp. 1841–1856, 2022.

[31] O. A. Hirose, "A Bayesian formulation of coherent point drift," *IEEE Trans. Pattern Anal. Mach. Intell.*, vol. 43, no. 7, pp. 2269–2286, Jul. 2021.

[32] Z. Yao, Q. Zhao, X. Li, and Q. Bi, "Point cloud registration algorithm based on curvature feature similarity," *Measurement*, vol. 177, 2021, Art. no. 109274.

[33] R. W. Sumner and J. Popović, "Deformation transfer for triangle meshes," *ACM Trans. Graph.*, vol. 23, no. 3, pp. 399–405, 2004.

[34] B. Amberg, S. Romdhani, and T. Vetter, "Optimal step nonrigid ICP algorithms for surface registration," in *Proc. IEEE Conf. Comput. Vis. Pattern Recognit.*, 2007, pp. 1–8.

[35] J. Yang, K. Li, K. Li, and Y.-K. Lai, "Sparse non-rigid registration of 3D shapes," *Comput. Graph. Forum*, vol. 34, no. 5, pp. 89–99, 2015.

[36] A. Chaudhury, "Multilevel optimization for registration of deformable point clouds," *IEEE Trans. Image Process.*, vol. 29, pp. 8735–8746, 2020.

[37] C. Jin, S. Li, and X. Yang, "Adaptive three-dimensional aggregate shape fitting and mesh optimization for finite-element modeling," *J. Comput. Civil Eng.*, vol. 34, no. 4, 2020, Art. no. 04020020.

[38] L. Cirrottola, M. Ricchiuto, A. Froehly, B. Re, A. Guardone, and G. Quaranta, "Adaptive deformation of 3D unstructured meshes with curved body fitted boundaries with application to unsteady compressible flows," *J. Comput. Phys.*, vol. 433, 2021, Art. no. 110177.

[39] O. Antepara, N. Balcázar, and A. Oliva, "Tetrahedral adaptive mesh refinement for two-phase flows using conservative level-set method," *Int. J. Numer. Methods Fluids*, vol. 93, no. 2, pp. 481–503, 2021.

[40] G. K. Matsopoulos, N. A. Mouravliansky, P. A. Asvestas, K. K. Delibasis, and V. Kouloulias, "Thoracic non-rigid registration combining self-organizing maps and radial basis functions," *Med. Image Anal.*, vol. 9, no. 3, pp. 237–254, 2005.

[41] P. Xi, W. Lee, and C. Shu, "In graphics, interface," *Anal. Segmented Hum. Body Scans*, pp. 19–26, 2007.

[42] P. Xi, W.-S. Lee, and C. Shu, "Analysis of segmented human body scans," in *Proc. Graph. Interfacew*, pp. 19–26, 2007.

[43] Q. Deng, M. Zhou, and Z. Wu, "An automatic non-rigid registration method for dense surface models," in *Proc. IEEE Int. Conf. Intell. Comput. Intell. Syst.*, 2010, pp. 888–892.

[44] J. Zhang, D. Ackland, and J. Fernandez, "Point-cloud registration using adaptive radial basis functions," *Comput. Methods Biomech. Biomed. Eng.*, vol. 21, no. 7, pp. 498–502, 2018.

[45] B. Amberg, S. Romdhani, and T. Vetter, "Optimal step nonrigid ICP algorithms for surface registration," in *Proc. IEEE Conf. Comput. Vis. Pattern Recognit.*, 2007, pp. 1–8.

[46] M. Dekker, *Mathematical Programming*, vol. 4. Boca Raton, FL, USA: CRC Press, 1986.

[47] F. Tajdari, M. Tajdari, and A. Rezaei, "Discrete time delay feedback control of stewart platform with intelligent optimizer weight tuner," in *Proc. IEEE Int. Conf. Robot. Automat.*, 2021, pp. 12 701–12 707.

[48] F. Tajdari and N. Ebrahimi Toulkani, "Implementation and intelligent gain tuning feedback–based optimal torque control of a rotary parallel robot," *J. Vib. Control*, vol. 28, no. 19/20, pp. 2678–2695, 2022.

[49] K. J. Åström and T. Hägglund, "PID controllers: Theory," *Des. Tuning*, vol. 2, pp. 59–120, 1995.

[50] A. Liu and B. Joe, "Relationship between tetrahedron shape measures," *BIT Numer. Math.*, vol. 34, no. 2, pp. 268–287, 1994.

[51] A. Visioli, *Practical PID Control*. Berlin, Germany: Springer, 2006.

[52] H. K. Khalil and J. W. Grizzle, *Nonlinear Systems*, vol. 3. Upper Saddle River, NJ, USA: Prentice Hall, 2002.

[53] K. M. Robinette, S. Blackwell, H. Daanen, M. Boehmer, and S. Fleming, "Civilian american and european surface anthropometry resource (caesar), final report. volume 1. summary," Sytronics Inc Dayton Oh, Tech. Rep. 2002-06-01, 2002.

[54] RUSSIAN3DSCANNER, Wrap 3.4, 2019. [Online]. Available: https://www.russian3dscanner.com/

[55] M. Tajdari et al., "Image-based modelling for adolescent idiopathic scoliosis: Mechanistic machine learning analysis and prediction," *Comput. Methods Appl. Mechanics Eng.*, vol. 374, 2021, Art. no. 113590.

[56] Sketchfab, "Thoracic-vertebrae 3D models," 2020. [Online]. Available: https://sketchfab.com/search?q=tag%3Athoracic-vertebrae&sort_by=-likeCount&type=models

[57] S. Valette, J. M. Chassery, and R. Prost, "Generic remeshing of 3D triangular meshes with metric-dependent discrete voronoi diagrams," *IEEE Trans. Vis. Comput. Graph.*, vol. 14, no. 2, pp. 369–381, Mar./Apr. 2008.

[58] J. R. Peters, C. Chandrasekaran, L. F. Robinson, S. E. Servaes, R. M. Campbell Jr, and S. Balasubramanian, "Age-and gender-related changes in pediatric thoracic vertebral morphology," *Spine J.*, vol. 15, no. 5, pp. 1000–1020, 2015.

[59] N. Charlie, "nricp - Non-rigid iterative closest point," 2020. [Online]. Available: https://www.mathworks.com/matlabcentral/fileexchange/54077-optimal-step-nonrigid-icp

[60] T. A. Davis, "Algorithm 832: Umfpack V4. 3—an unsymmetric-pattern multifrontal method," *ACM Trans. Math. Softw.*, vol. 30, no. 2, pp. 196–199, 2004.

[61] F. L. Lewis, D. Vrabie, and V. L. Syrmos, *Optimal Control*. Hoboken, NJ, USA: Wiley, 2012.

[62] R. L. Williams and D. A. Lawrence, *Linear Stat.-Space Control Systems*. Hoboken, NJ, USA: Wiley, 2007.

[63] F. Tajdari, C. Roncoli, and M. Papageorgiou, "Feedback-based ramp metering and lane-changing control with connected and automated vehicles," *IEEE Trans. Intell. Transp. Syst.*, vol. 23, no. 2, pp. 939–951, Feb. 2022.

[64] S. Tang and A. Godil, "An evaluation of local shape descriptors for 3D shape retrieval," in *Three-Dimensional Image Processing (3DIP) and Applications II*, vol. 8290. Bellingham, WA, USA: SPIE, 2012, Art. no. 82900N.

[65] F. Tajdari, A. Golgouneh, A. Ghaffari, A. Khodayari, A. Kamali, and N. Hosseinkhani, "Simultaneous intelligent anticipation and control of follower vehicle observing exiting lane changer," *IEEE Trans. Veh. Technol*, vol. 70, no. 9, pp. 8567–8577, Sep. 2021.

[66] F. Tajdari, N. E. Toulkani, and M. Nourimand, "Intelligent architecture for car-following behaviour observing lane-changer: Modeling and control," in *Proc. IEEE 10th Int. Conf. Comput. Knowl. Eng.*, 2020, pp. 579–584.

[67] F. Tajdari, A. Ghaffari, A. Khodayari, A. Kamali, N. Zhilakzadeh, and N. Ebrahimi, “Fuzzy control of anticipation and evaluation behaviour in real traffic flow,” in *Proc. 7th Int. Conf. Robot. Mechatron.*, 2019, pp. 248–253.

[68] MATLAB, *Fuzzy Membership Function in MATLAB*, 2019. [Online]. Available: https://www.mathworks.com/help/fuzzy/fismf.html

[69] A. Myronenko and X. Song, “Point set registration: Coherent point drift,” *IEEE Trans. Pattern Anal. Mach. Intell.*, vol. 32, no. 12, pp. 2262–2275, Dec. 2010.

[70] A. Myronenko and X. Song, “Executable source code,” 2010. [Online]. Available: https://github.com/markeroon/CoherentPointDrift

[71] O. Hirose, “Executable source code,” 2020. [Online]. Available: https://github.com/ohirose/bcpd

[72] V. G. Kim, Y. Lipman, and T. Funkhouser, “Blended intrinsic maps,” *ACM Trans. Graph.*, vol. 30, no. 4, 2011, Art. no. 79.

[73] H.-J. Wilke, V. M. Betz, and A. Kienle, “Morphometry of the kangaroo spine and its comparison with human spinal data,” *J. Anatomy*, vol. 238, no. 3, pp. 626–642, 2021.

Farzam Tajdari received the master’s degree in mechanical engineering from the Amirkabir University of Technology, Tehran, Iran, in 2016. He is currently working toward the PhD degree with the Faculty of Industrial Design Engineering, Delft University of Technology, Netherlands. He is also a postdoctoral researcher with the Mechanical Engineering department at TU Eindhoven, Netherlands. Currently, He is working on 3D scanning and ergonomics. His research interests include control, optimization, and non-linear systems to solve challenges in the fields of intelligent transportation systems, privacy of dynamic systems, and geometry processing.

Toon Huysmans received the PhD degree from the Department of Physics, University of Antwerp, Belgium. He currently is an assistant professor of Digital Human Modelling with the Faculty of Industrial Design Engineering of the Delft University of Technology. His main research interests are anthropometric and bio-mechanical digital human modelling and simulation with a focus on data-driven methods and design tools in the fields of ergonomics, anatomy, and orthopaedics. He has a specific interest in the design of ultra-personalised products and services.

Yu Song (Member, IEEE) received the PhD degree from the Department of Mechanical Engineering, The University of Hong Kong. He joined Faculty of Industrial Design Engineering, Delft University of Technology in 2001. He is currently an associate professor with the Department of Sustainable Design Engineering. His main research interests include human digital twin, 3D scanning and Ergonomics.